Universidade Federal de Juiz de Fora

Engenharia Elétrica

Programa de Pós-Graduação em Engenharia Elétrica

Lucas Giroto de Oliveira

Power Line Sensing via Power Line Communication-based Time-Domain Reflectometry

Juiz de Fora

2019

Lucas Giroto de Oliveira

Power Line Sensing via Power Line Communication-based Time-Domain Reflectometry

Dissertação de mestrado apresentada ao Programa de Pós-Graduação em Engenharia Elétrica da Universidade Federal de Juiz de Fora, na área de concentração em sistemas eletrônicos, como requisito parcial para obtenção do título de Mestre em Engenharia Elétrica.

Orientador: Prof. Moisés Vidal Ribeiro, Dr. Eng.
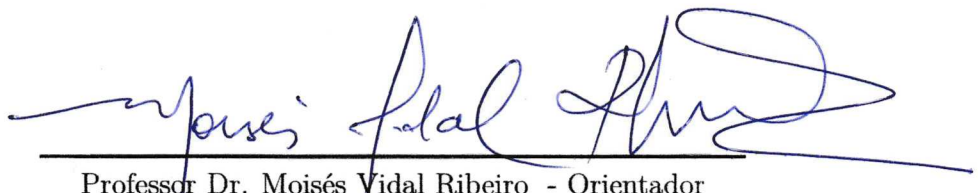
Juiz de Fora

2019

Lucas Giroto de Oliveira

Power Line Sensing via Power Line Communication-based Time-Domain Reflectometry

Dissertação de mestrado apresentada ao Programa de Pós-Graduação em Engenharia Elétrica da Universidade Federal de Juiz de Fora, na área de concentração em sistemas eletrônicos, como requisito parcial para obtenção do título de Mestre em Engenharia Elétrica.

Aprovada em: 20 de Março de 2019

BANCA EXAMINADORA

_____

Professor Dr. Moisés Vidal Ribeiro - Orientador
Universidade Federal de Juiz de Fora

_____

Professor Dr. Luciano Manhães de Andrade Filho
Universidade Federal de Juiz de Fora

_____

Professor Dr. Renato Machado
Instituto Tecnológico de Aeronáutica

ACKNOWLEDGEMENTS

"Imagination is more important than knowledge. For knowledge is limited, whereas imagination embraces the entire world, stimulating progress, giving birth to evolution."

Albert Einstein

RESUMO

Esta dissertação começa com uma discussão sobre a adequação de pulsos típicos de comunicação de linha de energia (PLC) para sensoriamento de redes de energia elétrica por refletometria no domínio do tempo (TDR) baseada em compressão de pulso. Para este propósito, um sistema de TDR é cuidadosamente descrito, discutindo suas limitações e, finalmente, recorrendo à compressão de pulso. Em seguida, são apresentadas expressões fechadas para pulsos e suas respectivas funções de autocorrelação para típicos esquemas de modulação de PLC. Além disso, a adequação dos pulsos PLC considerados para fornecer medições de TDR é discutida em termos de resolução, eficácia da compressão de pulso, distorção e alcance.

Em seguida, são discutidas as principais características e limitações de sistemas de TDR baseados no esquema de multiplexação Hermitiana simétrica por divisão de frequências ortogonais (HS-OFDM) para sensoriamento de redes de energia elétrica. Nesse sentido, um sistema de TDR baseado em HS-OFDM é descrito. Em seguida, as abordagens de processamento de reflectograma de compressão de pulso e estimação de canal são cuidadosamente descritas e os efeitos da parametrização do sistema de TDR e de esquemas de acesso múltiplo no desempenho do sistema de TDR baseado em HS-OFDM são abordados. Finalmente, um sistema de TDR baseado no esquema de multiplexação por divisão de *chirps* ortogonais (OCDM) é proposto para o sensoriamento de redes de energia elétrica. Após a descrição do modelo do sistema, é introduzido um esquema de acesso múltiplo que explora o teorema da convolução da transformação de Fresnel discreta modificada para permitir sensoriamento distribuído reflectométrico e transferométrico de redes de energia elétrica.

Uma análise numérica comparativa entre os pulsos PLC considerados é realizada para bandas de frequência que compreendem PLC de banda estreita (NB) - e banda larga (BB). Primeiramente, pulsos PLC são comparados em termos de número de refletogramas obtidos ao longo do tempo e qualidade do refletograma. É mostrado que os pulsos NB-PLC são adequados para a maioria dos cenários de rede de distribuição, sendo o uso de BB-PLC deixado para casos onde resoluções muito finas são desejadas. Análises numéricas adicionais são então apresentadas para apoiar a discussão realizada em sistemas de TDR multiportadoras com base nos esquemas HS-OFDM e OCDM. É mostrado que a estimação de canal supera a compressão de pulso para sistemas de TDR baseados em HS-OFDM. Uma comparação entre os esquemas de acesso múltiplo baseados em OCDM e HS-OFDM é então realizada. Os resultados numéricos mostram que o esquema de acesso múltiplo proposto baseado em OCDM resulta no maior número de medições ao longo do tempo, além de produzir a mesma resolução que seus pares baseados em HS-OFDM. Finalmente,

o esquema de acesso múltiplo baseado em OCDM é ligeiramente superado pelo HS-OFDM baseado no acesso múltiplo por divisão de código e pelo HS-OFDM baseado em acesso múltiplo por divisão de frequência em alguns modems de redes de energia elétrica que constituem o sistema de sensoriamento distribuído em termos de razão sinal-interferência-mais-ruído (SINR).

Palavras-chave: Sensoriamento de redes de energia elétrica. Reflectometria no domínio do tempo. Comunicação via rede de energia elétrica.

ABSTRACT

This thesis starts with a discussion on the suitability of typical power line communication (PLC) pulses for fault sensing in power lines via pulse-compression time-domain reflectometry (TDR). For this purpose, a TDR system is carefully outlined, discussing its limitations and ultimately resorting to pulse compression. Next, closed-form expressions for pulses and autocorrelation functions of typical PLC modulation schemes are presented. Furthermore, the suitability of the considered PLC pulses for providing proper TDR measurements is discussed in terms of resolution, effectiveness of the pulse compression, distortion, and range.

In sequel, key characteristics and limitations of TDR systems based on the Hermitian symmetric orthogonal frequency-division multiplexing (HS-OFDM) scheme for power line sensing are discussed. In this sense, a HS-OFDM based TDR system is outlined. Next, pulse compression and channel estimation reflectogram processing approaches are carefully described and the effects of TDR system parametrization and multiple access schemes on the HS-OFDM-based TDR system performance are addressed. Finally, a TDR system based on the orthogonal chirp-division multiplexing (OCDM) scheme is proposed for power line sensing. After the system model description, a multiple access scheme that exploits the convolution theorem of the modified discrete Fresnel transform for enabling distributed reflectometric and transferometric power line sensing is introduced.

A comparative numerical analysis among the considered PLC pulses is carried out for frequency bands comprising narrowband (NB)- and broadband (BB)-PLC. First, PLC pulses are compared in terms of number of obtained reflectograms over time and reflectogram quality. It is shown that NB-PLC pulses are suitable for most distribution network scenarios, being the use of BB-PLC left for cases where very fine resolutions are desired. Further numerical analyses are then presented for supporting the carried out discussion on multicarrier TDR systems based on both HS-OFDM and OCDM schemes. It is shown that channel estimation outperforms pulse compression for HS-OFDM-based TDR systems. A comparison among the OCDM- and HS-OFDM-based multiple access schemes is then performed. Numerical results show that the proposed OCDM-based multiple access scheme achieves the highest number of measurements over time, besides yielding the same range resolution as the HS-OFDM-based counterparts. Finally, the proposed OCDM-based multiple access scheme is slightly outperformed by the HS-OFDM based on code-division multiple access and by the HS-OFDM based on frequency-division multiple access at some power line modems consisting the distributed sensing system in terms of signal-to-interference-plus-noise ratio (SINR).

LIST OF FIGURES

LIST OF TABLES

ACRONYMS

8PSK eight phase-shift keying

ARIB Association of Radio Industries and Businesses

BB broadband

BPSK binary phase-shift keying

CDMA code-division multiple access

CENELEC European Committee for Electrotechnical Standardization (*Comité Européen de Normalisation Électrotechnique* in French)

CSS chirp spread spectrum

DFnT discrete Fresnel transform

DFT discrete Fourier transform

EMC electromagnetic compatibility

FCC Federal Communications Commission

FDMA frequency-division multiple access

FDR frequency-domain reflectometry

FFT fast Fourier transform

HIF high-impedance fault

HS-OFDM Hermitian symmetric orthogonal frequency-division multiplexing

HV high voltage

IDFnT inverse discrete Fresnel transform

IDFT inverse discrete Fourier transform

IFFT inverse fast Fourier transform

IoT Internet of Things

ISI intersymbol interference

ISLR integrated-sidelobe level ratio

JTFDR joint time-frequency domain reflectometry

LIF low-impedance fault

LPTV linear periodically time variant

LTI linear time-invariant

LV low voltage

MCTDR multicarrier time-domain reflectometry

MIMO multiple-input multiple-output

MTL multiconductor transmission line

MV medium voltage

NB narrowband

OCDM orthogonal chirp-division multiplexing

OFDM orthogonal frequency-division multiplexing

OMTDR orthogonal multitone time-domain reflectometry

PAPR peak-to-average power ratio

PCG pulse compression gain

PCR pulse compression ratio

PLC power line communication

PLM power line modem

PSD power spectral density

PSLR peak-to-sidelobe level ratio

QPSK quadrature phase-shift keying

SFR swept-frequency reflectometry

SG smart grid

SINR signal-to-interference-plus-noise ratio

SNR signal-to-noise ratio

TDMA time-division multiple access

TDR time-domain reflectometry

UWB ultra-wideband

WSS wide-sense stationary

TEM transverse electromagnetic

CONTENTS

1 INTRODUCTION

In the modern society, electrical energy is a paramount resource to both industry and residential consumers. Thus, the almost ubiquitous power transmission and distribution networks have been growing in size and complexity. The efficiency of such networks depends partly on their topology and partly on the physical characteristics and integrity of their components. The components of these networks are subjects to faults, which must be promptly handled in order to avoid interruptions in the power supply and consequent economic losses, besides avoiding public hazard.

Among the different types of faults in these networks are termination impedance changes, distributed faults and lumped faults [1]. The first are caused by either natural behavior of the loads or faults near the load, while the second are result of processes such as aging and degradation of cables. Lumped or localized faults, in their turn, are result of break of cables, as well as contact with threes or animals. The described factors generate low-impedance faults (LIFs) and high-impedance faults (HIFs), being the former easily detected by conventional protection schemes. The detection and location of HIFs, on the other hand, requires more careful approaches.

In the context of modern power line diagnosis, the use of higher frequencies than the mains has been widely considered in recently proposed techniques. A main reason for that is the high amount of information that can be extracted from the electric power network by monitoring harmonic voltages and currents [2,3], or even traveling waves [4] in a wider frequency band, thus allowing more efficient sensing of anomalies.

The use of the concept of traveling waves, widely used for sensing of wired networks, constitutes an attractive approach which has been gaining attention for detection and location of impedance discontinuities caused by elements such as branches, loads and faults [4]. For this purpose, wired networks are handled as transmission lines through which transverse electromagnetic (TEM) waves travel [5]. Important aplications of this concept are reflectometry techniques, which consist of injecting a pulse into the analyzed network and capturing the raised reflections that compose a *reflectogram* at a single measurement point by an instrument called *reflectometer*. As such signal propagates along the network, each impedance discontinuity causes part of the signal energy to be reflected and, through analysis of the reflected signal or *echo*, it is possible to obtain information on the network topology. Among different reflectometry approaches are the frequency-domain reflectometry (FDR), also known as swept-frequency reflectometry (SFR), and the time-domain reflectometry (TDR) [6]. There is also the joint time-frequency domain reflectometry (JTFDR), which benefits from the features from both FDR and TDR and overcomes some limitations associated with these approaches at the cost of more complex post-processing [7]. The difference among such techniques is mainly in the way of signal

injection, i.e., TDR consists of injecting a pulse that contains a broad spectral content, while classical FDR sequentially injects single-frequency signals until the whole desired frequency bandwidth is sensed. Such reflectometry techniques also differ in the reflectogram processing. For instance, TDR and FDR extract information from reflectograms in the time and frequency domains, respectively, while JTFDR extracts information in both domains via time-frequency analysis of reflectograms.

An interesting alternative for enabling reflectometric sensing of power lines is the use of power line communication (PLC) technology [8–16], which has proven to be a key technology in the context of smart grid (SG) [17–19] and also plays an important role in Industry 4.0, as it enables Internet of Things (IoT) applications that can perform industrial automation [20, 21]. The usage of a broad frequency bandwidth by PLC technologies empowers approaches based on traveling waves and enables the so-called *broadband reflectometry* [22], which provides reflectograms with finer resolution. In the specific case of power distribution networks, topics ranging from adjustments to power line modems (PLMs) for enabling network sensing [23] to machine learning-aided power line monitoring [24] have been investigated. Furthermore, approaches such as FDR-based techniques [25], combination of impedance and TDR techniques [26], as well as the use of JTFDR [7, 24] have been proposed.

The sole use of TDR principles for fault sensing in power lines, subject of study in the past [27, 28], has been recently revisited in the literature [29]. One of its main advantages is the reduced computational complexity due to simplified post-processing, as the reflectogram is almost directly obtained from the captured reflections. This characteristic allows on-line obtaining of reflectograms [30], efficiently enabling both symbol level sensing and mains level sensing [23].

In this context, there are many factors influencing the quality of reflectograms obtained by TDR systems, either based on classic pulse-compression TDR or the ones that exploit properties of multicarrier schemes. Also, more efficiency in terms of power line sensing can be achieved via distributed power line sensing, which demand the use of multiple access strategies.

1.1 OBJECTIVES

Given the aforementioned discussion and motivations, the main objectives of this thesis are summarized as follows:

- To investigate the use of typical PLC pulses for power line sensing via pulse-compression TDR. In this context, Hermitian symmetric orthogonal frequency-division multiplexing (HS-OFDM) [31], first [32] and second [33] derivatives of the Gaussian pulse (which belong to the impulsive ultra-wideband (UWB) category),

and chirp spread spectrum (CSS) [34] are considered. Also, range resolution, pulse compression ratio (PCR), peak-to-sidelobe level ratio (PSLR), integrated-sidelobe level ratio (ISLR), and maximum unambiguous range are introduced as performance metrics for pulse-compression TDR systems that make use of the aforementioned pulses.

- To exploit multicarrier properties of HS-OFDM-based TDR systems for power line sensing based on digital pulse compression and channel estimation reflectogram processing approaches. For this purpose, similar performance metrics to the aforementioned ones are adopted. Also, time-division multiple access (TDMA), frequency-division multiple access (FDMA), and code-division multiple access (CDMA) schemes are considered for enabling distributed power line sensing and compared in terms of signal-to-interference-plus-noise ratio (SINR) performance and number of measurements over time.

- To introduce an orthogonal chirp-division multiplexing (OCDM)-based TDR system for power line sensing that overcomes some of the limitations of its HS-OFDM-based counterparts. By exploiting the convolution theorem of a modified version of the discrete Fresnel transform (DFnT), on which such system is based, a multiple access scheme is introduced and compared with the HS-OFDM-based counterparts.

1.2 THESIS ORGANIZATION

The remainder of this document is organized as follows:

- Chapter 2 outlines the power line sensing system model. Based on transmission line theory, a power distribution network is modeled and the injection of signals and capture of raised reflections for ultimately forming a reflectogram is discussed.

- Chapter 3 discusses pulse-compression TDR for typical PLC pulses. Closed-form expressions for such pulses and their autocorrelation functions of typical PLC modulation schemes and performance metrics are presented for assessing reflectogram quality.

- Chapter 4 presents an HS-OFDM-based TDR system for power line sensing. In this chapter, digital pulse compression and channel estimation reflectogram processing approaches are compared, and the use of TDMA, FDMA, and CDMA schemes for enabling distributed power line sensing is discussed.

- Chapter 5 introduces an OCDM-based TDR system for power line sensing. Also, a multiple access scheme relying on the convolution theorem of the modified DFnT is proposed.

- Chapter 6 shows numerical analyses for supporting the carried out discussions in the previous chapters.

- Chapter 7 places concluding remarks of this thesis.

2 POWER LINE SENSING SYSTEM MODEL

This chapter outlines a system model for power line sensing via TDR, where a PLM works as a *reflectometer*. The PLM is therefore responsible for injecting signals and capturing reflections at a single measurement point of a power distribution network, ultimately forming a *reflectogram*. In this context, Section 2.1 describes the power line sensing system model, while Section 2.2 describes a fault sensing procedure for detecting and locating faults along a power distribution network provided that reflectograms are obtained under normal and fault conditions.

2.1 PROBLEM STATEMENT

First, let a power distribution network be constituted by power supply cable sections and branches ending at loads. From the perspective of transmission line theory, the power supply cable sections are approached as two-conductor transmission line sections with frequency-dependent characteristic impedance $Z_0(f)$ and propagation constant $\gamma(f)$, where f refers to frequency, which are determined by constructive characteristics of the power supply cable. The branches, in their turn, are bridged taps with finite length ending at a load. An example is the sketch of a single-phase power distribution network in Figure 1. In this figure, the power distribution network is constituted by a feeder, M line sections, and M branches ending at loads. The mth line section has length ℓ_m and the mth branch ends at a load with impedance $Z_{L,m}(f)$, where $m = 0, ..., M$. For the sake of simplicity, the variable f has been omitted in Figure 1.
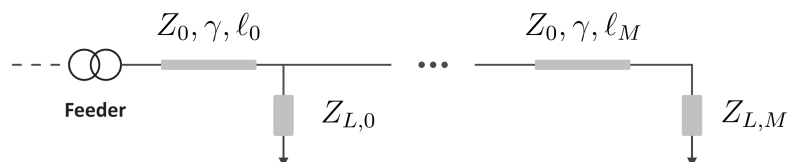
Figure 1: Sketch of a power distribution network under normal operation.

Next, let a full-duplex PLM be connected to a point of that power distribution network, experiencing an input impedance $Z_{in}(f)$ that results from the combination of the network elements [5]. Such transceiver injects pulses and captures their resulting reflections at a single measurement point as in Figure 2. Also, the use of an ideal circulator [35–37] is assumed, which completely separates the signals injected by the transmitting part of the PLM from the reflections captured by its receiving part. The combination of those elements therefore results in an linear periodically time variant (LPTV) impulse response $h(t,\tau)$ observed at the instant t given the injection of an impulse at $t - \tau$, where τ is a time lag, of the reflection channel experienced by the PLM connected to the network. Assuming that the injection and subsequent capture of reflections of signals takes place within a coherence time, in which variations in loads or any other element

of the network are irrelevant, one can consider that the distribution network is an linear time-invariant (LTI) system and denote its reflection channel impulse response simply as $h_\Gamma(t)$. Such assumption is made henceforth, being $h_\Gamma(t)$ considered to be deterministic throughout this thesis, although it could be considered a random process under certain circumstances.
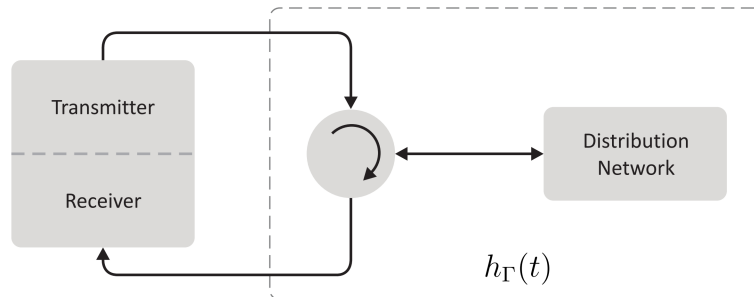
Figure 2: Reflectometry system over a power distribution network with impulse response $h_\Gamma(t)$ of the reflection channel.

The impulse response of the reflection channel $h_\Gamma(t)$, as its name suggests, is intimately related to reflections suffered by a signal propagating through the power distribution network, which are raised by impedance discontinuities along the power supply cable. Such reflections are quantified via the input reflection coefficient between the PLM of output impedance $Z_{PLM}(f)$ and the power distribution network of input impedance $Z_{in}(f)$, which is expressed as [5]

$$\Gamma_{in}(f) = \frac{Z_{in}(f) - Z_{PLM}(f)}{Z_{in}(f) + Z_{PLM}(f)}. \tag{2.1}$$

From $\Gamma_{in}(f)$, we finally obtain the impulse response of the reflection channel via the inverse Fourier transform, i.e.,

$$h_\Gamma(t) = \int_{-\infty}^{\infty} \Gamma_{in}(f) e^{j2\pi ft} df. \tag{2.2}$$

Alternatively, $h_\Gamma(t)$ can be expressed as

$$h_\Gamma(t) = \sum_{i=0}^{N_\Gamma-1} \alpha_i \delta(t - T_i), \tag{2.3}$$

where N_Γ is the number of impedance discontinuities experienced by the injected signal, while α_i and T_i are respectively the attenuation factor and the arrival time at the receiver side of the PLM associated with the reflection raised by the ith impedance discontinuity, $i \in \{0, \ldots, N_\Gamma - 1\}$.

The sensing of the power distribution network can therefore be performed via an analysis of the reflections raised by its impedance discontinuities. For this purpose, a TDR system operating is used for obtaining a reflectogram $\rho(t)$, which is an estimate of $h_\Gamma(t)$. Our TDR system operates on the system depicted in Figure 2. The transmitting part of

the PLM injects a pulse $s(t)$ into the power distribution network with reflection channel impulse response $h_\Gamma(t)$. This results in the reflected signal $\tilde{r}(t) = s(t) \star h_\Gamma(t)$, where $\star$ is the convolution operator. The captured signal by the receiver part of the PLM is composed by $\tilde{r}(t)$ plus an additive noise $v(t)$, which is a zero-mean wide-sense stationary (WSS) random process, and is represented by $r(t) = \tilde{r}(t) + v(t)$, or, alternatively,

$$r(t) = s(t) \star h_\Gamma(t) + v(t), \tag{2.4}$$

which is also a WSS random process. After further processing on $r(t)$, a reflectogram $\rho(t)$ is obtained. Consequently, $\rho(t)$ is also a WSS random process.

Among applications such as network topology inference [38,39], the reflectometric sensing of the power distribution network can be used for fault detection and location. Based on [25, 26, 40], a procedure for detecting and locating faults is described in the Section 2.2.

Given the described system, the TDR procedure aims to obtain a reflectogram $\rho(t)$ that is an appropriate estimate of $h_\Gamma(t)$. In order for this to happen, the ideal case would be $s(t) = \delta(t)$, where $\delta(t)$ is the Dirac delta function, and $v(t) = 0$. The corresponding continuous frequency-domain representation for $s(t)$ would therefore be, i.e., $S(f) = 1$, which denotes a zero-phase signal with constant magnitude in the continuous frequency-domain. In spite of such combination resulting in the best achievable estimate of $h_\Gamma(t)$, transmitting such an ideal signal and experiencing infinite signal-to-noise ratio (SNR), as practical TDR systems are band-limited and impaired by noise. Considering such systems, Chapter 3 discusses TDR systems whose transmit signals $s(t)$ are typical PLC pulses considering analog reflectogram processing. Next, Chapters 4 and 5 discuss multicarrier TDR systems with digital reflectogram processing and introduce multiple access schemes for enabling distributed power line sensing.

2.2 FAULT SENSING PROCEDURE

If no abnormality occurs in the power distribution network, i.e., its topology is just as depicted in Figure 1, it is said that the network is under normal operation conditions, presenting input impedance $Z_{in,normal}(f)$ and consequently input reflection coefficient $\Gamma_{in,normal}(f)$ and impulse response of the reflection channel $h_{normal}(t)$. However, if a localized fault with impedance $Z_{fault}(f)$ occurs, then the topology is changed to the one depicted in Figure 3. As a consequence, the input impedance of the power distribution network changes to $Z_{in,fault}(f)$ and additional reflections are suffered by the signal propagating in this network, resulting in an input reflection coefficient $\Gamma_{in,fault}(f)$ and an impulse response $h_{fault}(t)$ of the reflection channel. In addition to the normal reflections caused by impedance mismatchings and load connections already present in $h_{normal}(t)$,

the impulse response $h_{fault}(t)$ also encompasses reflections raised by the occurrence of the fault.
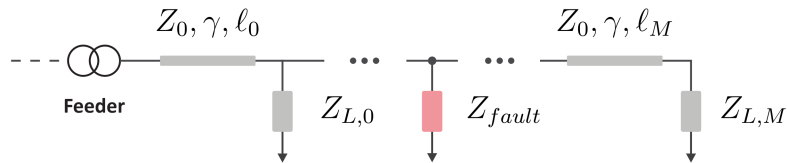
Figure 3: Sketch of a power distribution network under fault ocurrence.

Under normal and fault conditions, respectively, one obtains the reflectograms $\rho_{normal}(t)$ and $\rho_{fault}(t)$, which are weighted estimates of $h_{normal}(t)$ and $h_{fault}(t)$, respectively. A comparison of these reflectograms allows the identification of emerging impedance discontinuities in the latter reflectogram that were not present in the former. As $\rho_{normal}(t)$ and $\rho_{fault}(t)$ differ only for the reflections caused by the impedance discontinuity at the fault point, an appropriate parameter for evaluating fault occurrence is defined as

$$\Delta_\rho(t) = \rho_{fault}(t) - \rho_{normal}(t). \tag{2.5}$$

The fault detection problem resumes therefore to setting an amplitude threshold γ for $\Delta_\rho(t)$, above which reflections are considered to have been raised by a fault. For solving the fault location problem, one has

$$\Delta_\rho(d) = \Delta_\rho\left(\frac{v_p t}{2}\right), \tag{2.6}$$

where d is the distance in meters between the measurement point and the impedance discontinuity that caused the reflection, and v_p is the propagation velocity in m/s along the power supply cable. The factor $1/2$ relates to the actual distance of the impedance discontinuities from the measurement point to the round trip time of the observed reflections.

As previously mentioned, the occurrence of a fault causes multiple reflections, the first of them being the one that travels in a direct path from the fault point to the measurement point. The further reflections, in their turn, are raised when the former reflected signal passes by successive impedance discontinuities such as at load connection and branch points along its path. Hence, the fault location procedure consists of finding the position associated with the first peak of $\Delta_\rho(d)$ whose amplitude is above the threshold ξ. This results in an estimate of the distance from the fault to the measurement point, denoted by d_{fault} and expressed by

$$d_{fault} = \min\{d\}$$
$$\text{subject to}$$
$$\Delta_\rho(d) > \xi$$
$$\Delta\rho'(d) = 0, \tag{2.7}$$

where $\Delta'_\rho(d)$ is the derivative of $\Delta_\rho(d)$ with respect to d.

Among further fault location procedures, which can be used either as an alternative or a complement to the discussed procedure, are the use of machine learning [24] and time-reversal processing [41] approaches. While both these techniques can be used for adequately detecting and locating multiple faults, the former requires proper training data and the latter requires a complex model of the monitored network, usually based on transmission line theory.

3 ON THE SUITABILITY OF TYPICAL PLC PULSES FOR POWER LINE SENSING VIA TDR

The focus of this chapter is on pulse-compression TDR [30, 42], which consists of convolving the captured reflected signal with a matched filter to the injected pulse. Analyzing the resulting reflectogram, such procedure compresses the originally transmit signal into a narrower pulse, therefore performing resolution improvement and increasing the average transmitted power proportionally to the time duration of the originally injected pulse [42]. In contrast to typical studies on reflectometry-based sensing of wired networks, the aspects of resolution, range and quality of the obtained reflectograms are discussed by approaching the pulse-compression TDR in power lines as a *wired radar*, using metrics as range resolution, maximum unambiguous range, sidelobe level to assess the performance of the TDR system.

Given this context, this chapter describes TDR systems whose transmit signals are typical PLC pulses, i.e., HS-OFDM [31], first [32] and second [33] derivatives of the Gaussian pulse (which belong to the impulsive UWB category), and CSS [34], assuming an analog reflectogram processing approach. The remainder of this chapter is organized as follows. Section 3.1 formulates the problem for the considered TDR system. Section 3.2 discusses the compression of typical PLC pulses. Finally, Section 3.3 presents performance metrics for assessing the quality of obtained reflectograms.

3.1 PROBLEM STATEMENT

When obtaining a reflectogram, it is desired to have a transmit pulse $s(t)$ that is sufficiently narrow to provide a fair approximation of $\delta(t)$ and therefore adequate temporal and consequently spatial resolution for the reflectogram $\rho(t)$. It is also desired to have a high transmission power, so that the receiving part of the reflectometer experiences an adequate SNR.

A first approach to meet those requirements in a band-limited system is to send a narrow pulse, with well-defined main lobe and sidelobes. As it is desired to have $s(t)$ that approximates $\delta(t)$, the side lobes should present significantly lower amplitude than the main lobe to avoid undesirable distortions in the reflectogram. Although this would allow practical implementation, one would have a transmit pulse $s(t)$ with high peak-to-average power ratio (PAPR), i.e., great part of its energy would be concentrated in a short time interval corresponding to the main lobe of the transmit pulse. This may be undesired, since there are upper bounds on the maximum amplitude of the transmit pulse due to hardware limitations and regulatory constraints.

A solution to this issue is transmitting a longer $s(t)$ that can present lower PAPR, i.e., does not need to present well-defined main lobe and sidelobes, and then performing

processing on the received signal $r(t)$ to obtain the reflectogram $\rho(t)$. This processing, called pulse compression [42–44], artificially turns the originally transmit pulse $s(t)$ into a narrow pulse with high PAPR that in its turn approximates $\delta(t)$, improving the resolution and increasing the SNR of the reflectogram $\rho(t)$.

For describing the pulse compression procedure, let the transmit pulse $s(t)$ be expressed as the normalization of a pulse $p(t)$ by its 2-norm, followed by a multiplication by an energy factor, i.e.,

$$s(t) = \sqrt{E}\frac{p(t)}{\|p(t)\|}, \tag{3.1}$$

where E is the energy of $s(t)$ and $\|\cdot\|$ returns the 2-norm of a signal. Therefore, the pulse compression procedure consists of performing the convolution of the received signal $\rho(t)$ with a pulse compression filter whose impulse response is $p^*(-t)/\|p^*(-t)\|$, where $(\cdot)^*$ is the complex conjugate operator. The result of such operation is the reflectogram, which can be expressed as

$$
\begin{aligned}
\rho(t) &= r(t) \star \frac{p^*(-t)}{\|p^*(-t)\|} \\
&= \left(\sqrt{E}\frac{p(t)}{\|p(t)\|} \star h_\Gamma(t)\right) \star \frac{p^*(-t)}{\|p^*(-t)\|} + v(t) \star \frac{p^*(-t)}{\|p^*(-t)\|}.
\end{aligned} \tag{3.2}
$$

Knowing that

$$
\begin{aligned}
R_{pp}(\tau) &= \int_{-\infty}^{\infty} p(t)p^*(t-\tau)dt \\
&= p(t) \star p^*(-t)|_{t=\tau}
\end{aligned} \tag{3.3}
$$

is the autocorrelation function of the deterministic energy signal $p(t)$ at the time lag τ [43], one can write

$$\rho(t) = \frac{\sqrt{E}}{\|p(t)\|^2}R_{pp}(\tau) \star h_\Gamma(t) + v(t) \star \frac{p^*(-t)}{\|p^*(-t)\|}. \tag{3.4}$$

As the autocorrelation of a signal is pulse-shaped, one can easily see from (3.4) that the pulse compression filter is used with the purpose of compressing $p(t)$ into the pulse $R_{pp}(\tau)$, which is depicted in Figure 4. As $R_{pp}(\tau) = p(t) \star p^*(-t)|_{t=\tau}$, its resulting continuous frequency-domain representation is $R_{pp}(f) = P(f)P^*(f)$, where $P(f)$ is the continuous frequency-domain representation of $p(t)$. Alternatively,

$$R_{pp}(f) = |P(f)|^2, \tag{3.5}$$

which is a zero-phase signal and can be designed in order to approximate the ideal scenario of a flat continuous frequency-domain representation described in Chapter 2.

If $R_{pp}(\tau)$ has a sufficiently narrow main lobe and sidelobes with sufficiently low amplitude, then it can be assumed that

$$\rho(t) \approx \frac{\sqrt{E}}{\|p(t)\|^2}h_\Gamma(t) + v(t) \star \frac{p^*(-t)}{\|p^*(-t)\|}. \tag{3.6}$$
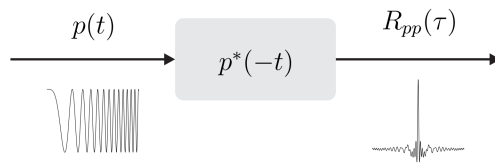
Figure 4: Pulse compression.

It can be seen that the first term of the sum from (3.6) is a weighted version of $h_\Gamma(t)$, while the second term refers to the noise component. Despite having its amplitude altered over time, the noise component will have the same power, as it is convolved with the unit-power compression filter.

Based on the carried-out discussion, one can easily conclude that the quality of a reflectogram will depend upon two main factors, namely *(i)* how well $R_{pp}(\tau)$ approximates $\delta(t)$, i.e., how adequate the estimate of $h_\Gamma(t)$ is, and *(ii)* the SNR level, which drives the performance of the threshold detector previously described. The former depends only on the transmit pulse's characteristics, while the latter depends on both the effectiveness of the pulse compression procedure and the additive noise characteristics. The focus of this chapter is on aspects of the reflectogram that do not depend on specific system's conditions such as noise, being therefore the sole investigation of autocorrelation functions of typical PLC pulses our subject of study. In this sense, expressions for $R_{pp}(\tau)$ of such signals are derived in Section 3.2 for enabling an assessment of their suitability for TDR purposes.

3.2 COMPRESSION OF PLC PULSES

In this section, pulses of four commonly adopted modulation techniques for PLC systems are presented and their autocorrelation functions are derived to determine whether they are suitable for TDR purposes.

3.2.1 Hermitian-Symmetric OFDM

Let an HS-OFDM system transmit a complex symbol $\mathbf{P} = [P_0, P_1, \ldots, P_{N-1}]$, where $P_k \in \mathbb{C}$, $k \in \{0, \ldots, N-1\}$. By performing an Hermitian symmetric mapping [31] on $\mathbf{P}$ before digital-to-analog conversion, the transmit pulse in the continuous time-domain can be expressed as

$$p_{OFDM}(t) = \Re\{P_{N-1}\}e^{j2\pi 0\Delta ft} + \sum_{k=0}^{N-2}\left(P_k e^{j2\pi k\Delta ft} + P_k^* e^{-j2\pi k\Delta ft}\right) + \Im\{P_{N-1}\}e^{j2\pi N\Delta ft},$$

(3.7)

where $-T/2 < t < T/2$, with T denoting the pulse duration, $\Delta f = 1/T$ is the subcarrier frequency spacing, and $\Re\{\cdot\}$ and $\Im\{\cdot\}$ respectively denote the real and imaginary parts of

a complex number. An analysis of (3.7) reveals that $p(t)$ occupies a frequency bandwidth equal to

$$B_{OFDM} = N\Delta f, \tag{3.8}$$

i.e., it ranges from $-B_{OFDM}$ to B_{OFDM} in the continuous frequency-domain.

Assuming uniform power allocation and binary phase-shift keying (BPSK) modulation, it holds that $P_k \in \mathbb{R}, \forall n$. This results in $|P_k| = \sqrt{E}$, as well as in $P_k = P_k^*$ and $\Im\{P_{N-1}\} = 0$. Therefore, the autocorrelation function of $p(t)$ for an HS-OFDM system is defined for $-T < t < T$ as in (3.9).

$$
\begin{aligned}
R_{pp,OFDM}(\tau) \; \stackrel{\triangle}{=} \; & P_{N-1}^2 (2T - |\tau|) + P_{N-1} \sum_{l=0}^{N-2} P_l \left(\frac{\sin(2\pi l \Delta f T) + \sin[2\pi l \Delta f(T - |\tau|)] + \sin[2\pi l \Delta f(2T - |\tau|)]}{\pi \Delta f l} \right) \\
& + \sum_{l=0}^{N-2} \sum_{m=0}^{N-2} P_l P_m \left(\frac{\sin[2\pi l \Delta f(T - |\tau|)] + \sin[2\pi m \Delta f(T - |\tau|)]}{\pi \Delta f(l + m)} + \frac{\sin[2\pi l \Delta f(T - |\tau|)] - \sin[2\pi m \Delta f(T - |\tau|)]}{\pi \Delta f(l - m)} \right)
\end{aligned}
\tag{3.9}
$$

Figs. 5a and 5b show respectively the normalized pulse and its normalized autocorrelation for the HS-OFDM scheme. In this figure, the normalized HS-OFDM pulse and its autocorrelation function are respectively given by $\overline{p}_{OFDM}(t) = p_{OFDM}(t)/\max\{|p_{OFDM}(t)|\}$ and $\overline{R}_{p,OFDM}(\tau) = R_{pp,OFDM}(\tau)/\max\{|R_{pp,OFDM}(\tau)|\}$, where $\max\{\cdot\}$ returns the maximum value of a signal. This normalization will also be performed for presenting the pulses and their autocorrelations for the remaining cases.
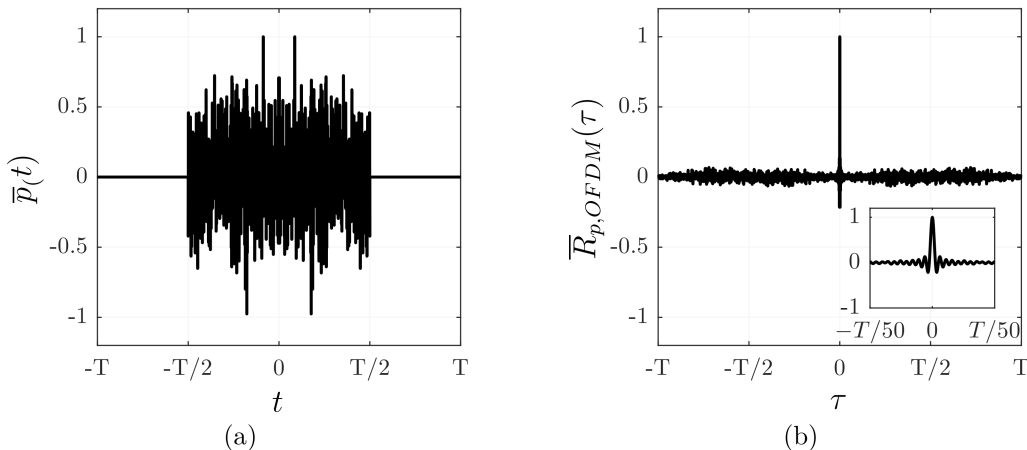
Figure 5: HS-OFDM pulse: (a) $\overline{p}_{OFDM}(t)$ and (b) its autocorrelation $\overline{R}_{p,OFDM}(\tau)$.

3.2.2 Ultra-Wideband

For the UWB system, the first [32] and second [33] derivatives of the Gaussian pulse with respect to t are considered, i.e., $g'(t)$ and $g''(t)$, where $g(t)$ is the Gaussian pulse. The Gaussian pulse is defined for $-T/2 < t < T/2$ and is expressed in the continuous time-domain as

$$g(t) = \frac{1}{\sqrt{2\pi}\sigma}e^{-\frac{1}{2}\left(\frac{t}{\sigma}\right)^2},$$ (3.10)

with σ denoting the variance.

3.2.2.1 First derivative of the Gaussian pulse

The first derivative of the Gaussian pulse is expressed in the continuous time-domain as

$$p_{UWB-1}(t) = -\frac{t}{\sqrt{2\pi}\sigma^3}e^{-\frac{1}{2}\left(\frac{t}{\sigma}\right)^2}.$$ (3.11)

Besides $p_{UWB-1}(t)$ being defined for $-T/2 < t < T/2$, its effective duration is $T = 7\sigma$ [45]. The occupied frequency bandwidth by $p_{UWB-1}(t)$ is defined as the lowest frequency beyond which its continuous frequency-domain representation $P_{UWB-1}(f)$ is at least 30 dB below its maximum value [33]. Based on this assumption, one has a continuous frequency-domain representation ranging from $-B_{UWB-1}$ to B_{UWB-1}, in which

$$B_{UWB-1} \approx \frac{1599.49 \times 10^{-3}}{\pi\sigma}.$$ (3.12)

The autocorrelation function of $p_{UWB-1}(t)$ for the first derivative of the Gaussian pulse is therefore given by

$$R_{pp,UWB-1}(\tau) = \frac{-1}{8\sqrt{\pi}\sigma^5}\left(\tau^2 - 2\sigma^2\right)e^{-\frac{\tau^2}{4\sigma^2}} \tag{3.13}$$

and is defined for $-T < \tau < T$, or, alternatively, $-7\sigma < \tau < 7\sigma$.

Figs. 6a and 6b show respectively the normalized pulse $\overline{p}_{UWB-1}(t)$ and its normalized autocorrelation $\overline{R}_{p,UWB-1}(\tau)$ for the first derivative of the Gaussian pulse.
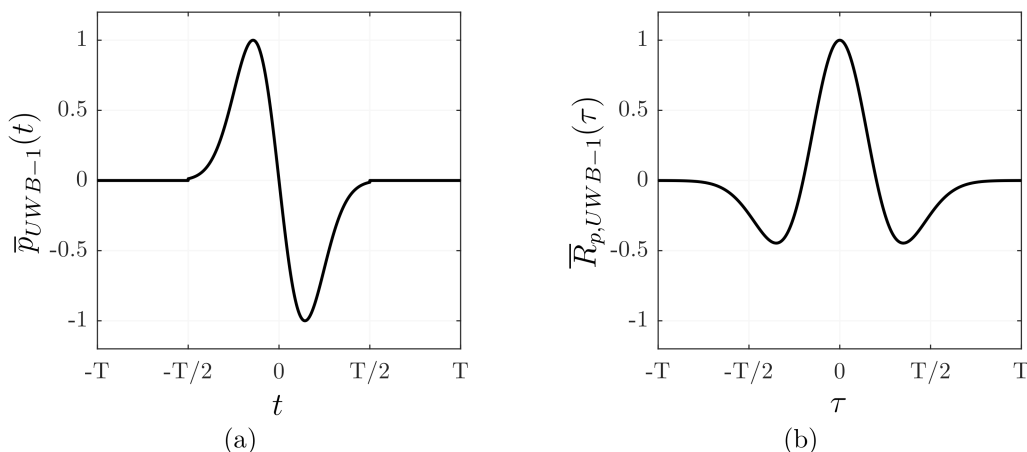
Figure 6: First derivative of the Gaussian pulse: (a) $\overline{p}_{UWB-1}(t)$ and (b) its autocorrelation $\overline{R}_{p,UWB-1}(\tau)$.

3.2.2.2 Second derivative of the Gaussian pulse

The second derivative of the Gaussian pulse is expressed in the continuous time-domain as

$$p_{UWB-2}(t) = \frac{t^2 - \sigma^2}{\sqrt{2\pi}\sigma^5}e^{-\frac{1}{2}\left(\frac{t}{\sigma}\right)^2}. \tag{3.14}$$

and is defined for $-T/2 < t < T/2$, with $T = 7\sigma$ as in the case of $p_{UWB-1}(t)$. Adopting the same criterion from the previous UWB pulse, the occupied frequency bandwidth by $p_{UWB-2}(t)$ is given by

$$B_{UWB-2} \approx \frac{564.65 \times 10^{-3}}{\sigma}, \tag{3.15}$$

i.e., its continuous frequency-domain representation ranges from $-B_{UWB-2}$ to B_{UWB-2}.

By convolving $p_{UWB-2}(t)$ with $p^*_{UWB-2}(-t)$, one obtains the autocorrelation function of $p_{UWB-2}(t)$ for the second derivative of the Gaussian pulse, expressed as

$$R_{pp,UWB-2}(\tau) = \frac{1}{32\sqrt{\pi}\sigma^9}\left(\tau^4 - 12\sigma^2\tau^2 + 12\sigma^4\right)e^{-\frac{\tau^2}{4\sigma^2}}, \tag{3.16}$$

which is defined for $-T < \tau < T$, or, alternatively, $-7\sigma < \tau < 7\sigma$.

Figs. 7a and 7b show respectively the normalized pulse $\overline{p}_{UWB-2}(t)$ and its normalized autocorrelation $\overline{R}_{p,UWB-2}(\tau)$ for the second derivative of the Gaussian pulse.
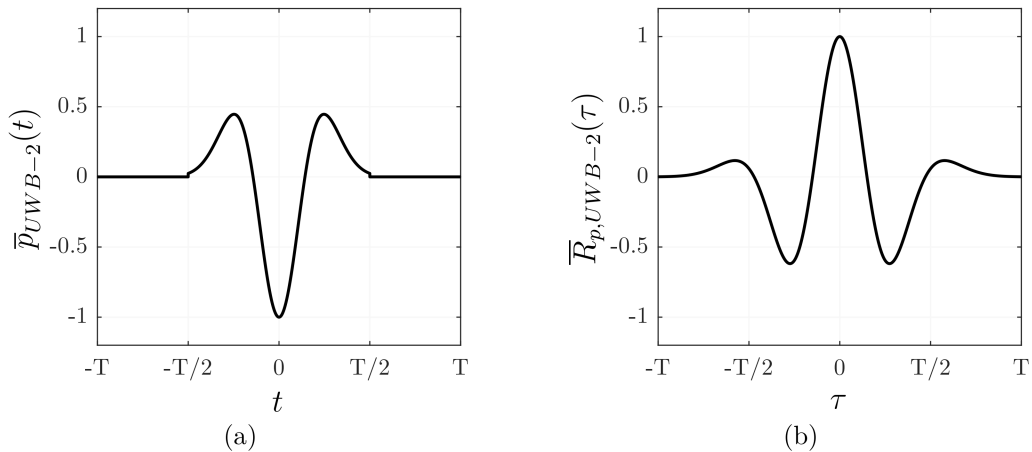
Figure 7: Second derivative of the Gaussian pulse: (a) $\overline{p}_{UWB-2}(t)$ and (b) its autocorrelation $\overline{R}_{p,UWB-2}(\tau)$.

3.2.3 Chirp Spread Spectrum

The baseband CSS system multiplies an up- or down-chirp $p_{CSS}(t)$, properly normalized to present unit power, by a factor $\sqrt{E}$ before transmitting it. In this chapter, the baseband up-chirp is defined for $-T/2 < t < T/2$ and denoted in the continuous time-domain by

$$p_{CSS}(t) = \cos(\pi\mu t^2). \tag{3.17}$$

where $\mu \in \mathbb{R}$ is the chirp rate. For a given μ value, the occupied frequency bandwidth by $p_{CSS}(t)$ is given by

$$B_{CSS} = |\mu|\frac{T}{2}, \tag{3.18}$$

which results in the fact that $p_{CSS}(t)$ linearly sweeps frequencies from $-B_{CSS}$ to B_{CSS} in T seconds.

By convolving $p_{CSS}(t)$ with its matched counterpart $p^*_{CSS}(-t)$, one obtains $R_{pp,CSS}(\tau)$, which is defined for $-T < \tau < T$ and is defined as

$$R_{pp,CSS}(\tau) \triangleq \Lambda(T/2,\tau) - \Lambda(-T/2,\tau) + \frac{1}{2\pi\mu\tau}\cos(\pi\mu\tau^2)\sin(\pi\mu\tau T), \tag{3.19}$$

with

$$\Lambda(t,\tau) \triangleq \frac{1}{4\sqrt{\mu}}\left[\cos\left(\frac{\pi\mu\tau^2}{2}\right)\mathcal{C}\left(\sqrt{\mu}(2t-\tau)\right) - \sin\left(\frac{\pi\mu\tau^2}{2}\right)\mathcal{S}\left(\sqrt{\mu}(2t-\tau)\right)\right], \tag{3.20}$$

where $\mathcal{C}(\cdot)$ and $\mathcal{S}(\cdot)$ denote, respectively, the Fresnel cosine and Fresnel sine integrals as in their second definition in [46]. Figs. 8a and 8b show respectively the normalized pulse $\overline{p}_{CSS}(t)$ and its normalized autocorrelation $\overline{R}_{p,CSS}(\tau)$ for the considered up-chirp pulse.
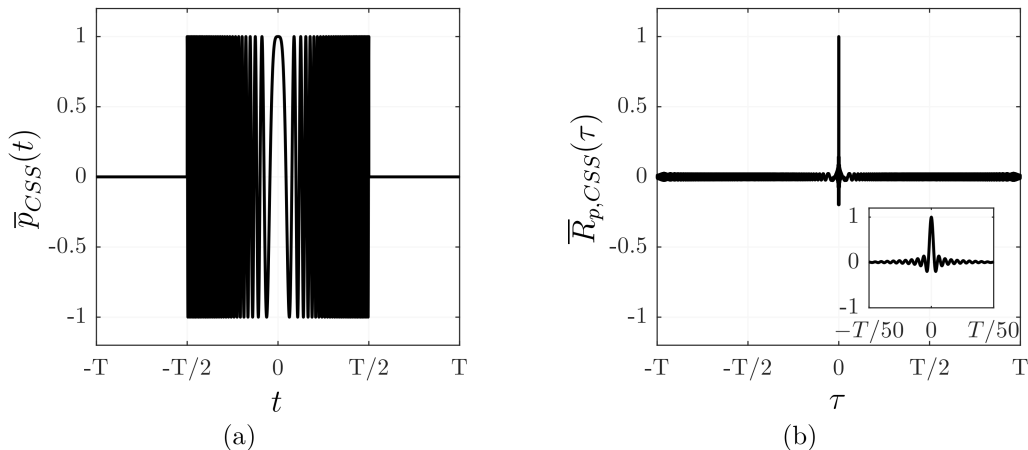
Figure 8: CSS pulse: (a) $\overline{p}_{CSS}(t)$ and (b) its autocorrelation $\overline{R}_{p,CSS}(\tau)$.

3.3 REFLECTOGRAM QUALITY

Disregarding noise effect, the quality of the estimate of $h_\Gamma(t)$ provided by the reflectogram $r(t)$ according to (3.6) can be assessed by means of different metrics. These metrics can be used for evaluating the range resolution of the reflectometry system, which is the capability of resolving subsequent reflections, as well as the pulse compression effectiveness and the reflectogram distortion caused by the sidelobes of the transmit pulse's autocorrelation function.

3.3.1 Range Resolution

The adopted metric for evaluating the range resolution is the Rayleigh criterion, widely used in radar systems [43]. Given a pulse with main lobe width of $2T_{\Delta d}$ as shown in Figure 9a, this criterion states that reflections related to two impedance discontinuities with spacing Δd from one another are only resolved if the peak of the main lobe of one reflections falls at the same time instant as a zero crossing immediately next to the main lobe of the other reflection, i.e., the reflections are spaced in time by $T_{\Delta d} = \Delta d/(v_p/2)$, as depicted in Figure 9b. This criterion can be used as a metric for comparing the resolution of reflectograms obtained via transmit pulses with different autocorrelation functions.

The range resolutions associated to the autocorrelation $R_{pp,i}(\tau)$, $i \in \{OFDM, UWB - 1, UWB - 2, CSS\}$, is therefore the product of the time instant of the first positive zero crossing of $R_{pp,i}(\tau)$ by $v_p/2$, i.e., $\Delta d_i = v_p T_{\Delta d,i}/2$. Finding the first zero crossings of $R_{pp,i}(\tau)$ resumes to solving $R_{pp,i}(\tau) = 0$ for τ, setting $T_{\Delta d,i}$ as the smallest absolute value of τ obtained, and multiplying it by $v_p/2$. The range resolutions for HS-OFDM, UWB and CSS pulses are presented as follows:
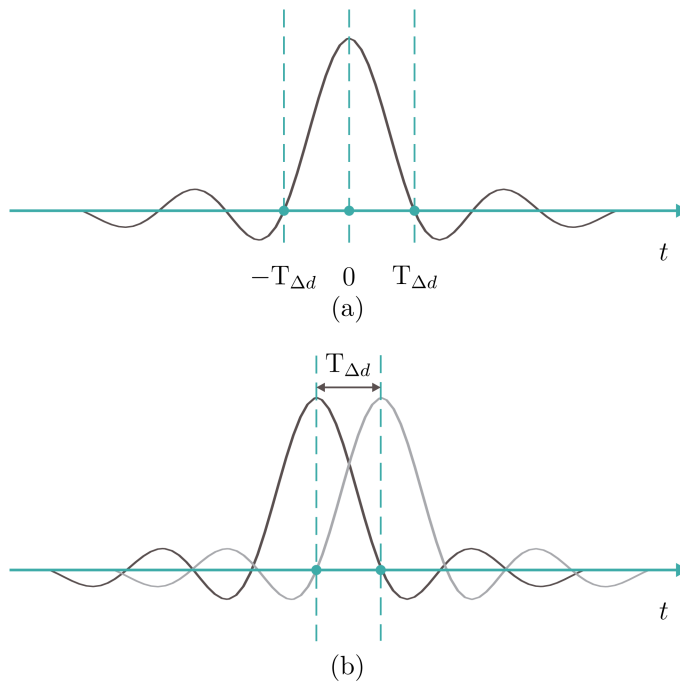
Figure 9: Autocorrelation function $R_{pp}(\tau)$: (a) zero crossings and (b) Rayleigh resolution.

3.3.1.1 Range Resolution of HS-OFDM Pulse

For the HS-OFDM pulse with uniform power allocation, $\mathrm{T}_{\Delta d,OFDM}$ is obtained by equaling (3.9) to zero, yielding $\mathrm{T}_{\Delta d,OFDM} = 1/(2B_{OFDM})$ [30,47]. Multiplying the result of this procedure by $v_p/2$, one obtains the range resolution $\Delta d_{OFDM} = v_p \mathrm{T}_{\Delta d,OFDM}/2$, expressed as

$$\Delta d_{OFDM} = \frac{v_p}{4B_{OFDM}}. \tag{3.21}$$

3.3.1.2 Range Resolution of Ultra-Wideband Pulses

Regarding UWB pulses, the Rayleigh resolution $\Delta d_{UWB-1} = v_p \mathrm{T}_{\Delta d,UWB-1}/2$ for the first derivative of the Gaussian pulse is obtained by equaling (3.13) to zero and solving for τ, which yields $\mathrm{T}_{\Delta d,UWB-1} = \sqrt{2}\sigma$. Multiplying this result by $v_p/2$, one gets

$$\Delta d_{UWB-1} = \frac{v_p \sigma}{\sqrt{2}}. \tag{3.22}$$

For the second derivative of the Gaussian pulse, it holds that $\mathrm{T}_{\Delta d,UWB-2} = \sigma\sqrt{6 - 2\sqrt{6}}$ via the same procedure for the previous case. The Rayleigh resolution $\Delta d_{UWB-2} = v_p \mathrm{T}_{\Delta d,UWB-2}/2$ is then

$$\Delta d_{UWB-2} = \frac{v_p}{2}\sigma\sqrt{6 - 2\sqrt{6}}. \tag{3.23}$$

3.3.1.3 Range Resolution of CSS Pulse

For the CSS case, the expression $R_{pp,CSS}(\tau) = 0$ must be solved numerically for τ and no closed-form expression for Δd_{CSS} could be presented in this case. However,

by making use of an approximation for linear chirps with $B_{CSS}T > 10$ reported in the literature [43], one obtains $T_{\Delta d,CSS} \approx 1/(2B_{CSS})$ and the range resolution $\Delta d_{CSS} = v_p T_{\Delta d,CSS}/2$, which is expressed as

$$\Delta d_{CSS} \approx \frac{v_p}{4B_{CSS}}. \tag{3.24}$$

3.3.2 Pulse compression ratio

Once the range resolution has been obtained, the effectiveness of the pulse compression can be evaluated by means of the PCR [48], which is a ratio between the pulse length before pulse compression and the effective pulse length after the compression procedure, i.e., $T_{\Delta d,i}$

$$PCR_i = \frac{T}{T_{\Delta d,i}}, \tag{3.25}$$

with $i \in \{OFDM, UWB-1, UWB-2, CSS\}$.

The PCR can alternatively be interpreted as a ratio between the effective average power of a pulse compression TDR system and a simple pulse system, provided that peak power and range resolution is the same for both cases [48]. Depending on the noise characteristics, PCR can be used for measuring SNR gain provided by the pulse compression procedure, being also known as pulse compression gain (PCG) [43]. Given this context, the PCRs for HS-OFDM, UWB and CSS pulses are presented as follows:

3.3.2.1 Pulse compression ratio of HS-OFDM pulse

Given the $T_{\Delta d,OFDM}$ value obtained in Subsection 3.3.1.1, the PCR for the HS-OFDM pulse is

$$PCR_{OFDM} = 2B_{OFDM}T. \tag{3.26}$$

3.3.2.2 Pulse compression ratio of Ultra-Wideband pulses

For the first derivative of the Gaussian pulse, which presents $T_{\Delta d,UWB-1}$ as shown in Subsection 3.3.1.2, one has

$$PCR_{UWB-1} = \frac{7}{\sqrt{2}} \approx 4.95, \tag{3.27}$$

while the associated PCR with the second derivative of the Gaussian pulse is

$$PCR_{UWB-2} = \frac{7}{\sqrt{6 - 2\sqrt{6}}} \approx 6.67, \tag{3.28}$$

both results holding for any given $T = 7\sigma$.

3.3.2.3 Pulse compression ratio of CSS pulse

The $T_{\Delta d, CSS}$ value obtained in Subsection 3.3.1.3 for the CSS pulse results in a PCR given by

$$PCR_{CSS} \approx 2B_{CSS}T. \tag{3.29}$$

3.3.3 Reflectogram distortion

Further metrics can be used for assessing the quality of the reflectogram in terms of distortion caused by the presence of sidelobes in the autocorrelation function of the transmit pulse. In this chapter, PSLR and ISLR [47] are the adopted metrics for this purpose. The PSLR measures the ratio between the highest sidelobe and the main lobe, i.e.,

$$PSLR = \frac{\max_{\tau \neq 0} \{|R_{pp}(\tau)|\}}{|R_{pp}(0)|}. \tag{3.30}$$

In its turn, the ISLR measures the ratio between the integration of the sidelobes and the main lobe, which can be expressed as

$$ISLR = \frac{\int_{-\infty}^{-T_\delta} |R_{pp}(\tau)| \, d\tau + \int_{T_\delta}^{\infty} |R_{pp}(\tau)| \, d\tau}{\int_{-T_\delta}^{T_\delta} |R_{pp}(\tau)| \, a d\tau}, \tag{3.31}$$

where $|\cdot|$ is the absolute value operator.

Pulses that present high PSLR and/or ISLR values can cause significant distortion in the reflectogram if used for TDR purposes. However, it is possible to mitigate such undesired effect with signal processing techniques. Among widely used approaches are either windowing the reflectogram, which reduces the level of sidelobes with the drawbacks of SNR reduction and broadening of the main lobe [30, 43, 44], or designing pulses with desired autocorrelations.

3.3.4 Maximum Unambiguous Range

Besides assessing the quality of the reflectogram in terms of resolution and distortion, it is also important to determine the distance interval within which there is no interference between reflectograms of subsequent pulses. Such interval is named maximum unambiguous range and is related to the maximum duration of the reflection channel $h_\Gamma(t)$, denoted by $T_{h,\max}$, supported by the reflectometry system.

For this purpose, the pulse repetition interval is defined as the time interval between subsequent pulse injections [43, 48] down to the distribution network and denote it by ΔT_p. The maximum duration of $h_\Gamma(t)$ is defined based on the fact that the maximum duration of the complete echo response $\rho(t)$, denoted by $T_{\rho,\max}$, is equal to ΔT_p. As $\rho(t)$ is the result of the convolution between $s(t)$ and $h_\Gamma(t)$, one has $T_{\rho,\max} = T + T_{h,\max}$

and, therefore, $T_{h,\max} = \Delta T_p - T$. As a consequence, the maximum unambiguous range from the measurement point is given by $d_{\max} = v_p T_{h,\max}/2$, i.e.,

$$d_{\max} = \frac{v_p \left(\Delta T_p - T\right)}{2}.$$

(3.32)

It is clear from this expression that the maximum unambiguous range depends upon not only on the duration of the adopted pulse, but also on the periodicity in which it is injected into the channel. An appropriate reflectometry system must therefore consider the duration of a given $h_\Gamma(t)$ in order to define a T and ΔT_p pair that does not cause interference between reflectograms.

4 HERMITIAN-SYMMETRIC OFDM FOR POWER LINE SENSING VIA TDR

As described in Chapter 3, appropriate power line sensing can be performed via an adequate parametrization of the TDR system based on analog reflectogram processing. However, more effectiveness in terms of signal processing and electromagnetic compatibility (EMC) without the inherent drawback of poor spectrum control in classical TDR can be achieved by multicarried-based TDR, in which digital reflectogram processing is performed. In this context, multicarrier time-domain reflectometry (MCTDR) [49, 50] and its time-domain version [51], which only differ in the domain where reflectogram processing takes place, have been introduced. For enhanced compatibility with existing PLC systems and optimized digital signal processing, an interesting approach is the orthogonal multitone time-domain reflectometry (OMTDR) [30], which is variation of the MCTDR based on orthogonal frequency-division multiplexing (OFDM).

Although TDR based on OFDM or its baseband version HS-OFDM seems a good candidate for power line sensing, aspects such as measurement range and number of reflectograms obtained over time become more relevant due to the long distances in power distribution networks and the LPTV behavior of transfer functions experienced by signals injected by PLMs into the network. Also, the use of channel estimation, performed for communication purposes in PLC systems [52], rather than the usual pulse compression performed for reflectometric sensing in wired networks [30, 42] has not yet been addressed in the literature. For an efficient distributed sensing, the effect of multiple access on TDR measurements, already considered for pulse compression TDR in some aspects [30, 53], must also be taken into account for HS-OFDM-based TDR systems relying on channel estimation.

Given this context, the influences of the parametrization of an HS-OFDM-based TDR system as well as limitations imposed by multiple access schemes on its performance for power line sensing are discussed in this chapter. The remainder of this chapter is organized as follows. Section 4.1 describes the HS-OFDM-based TDR system for sensing of a power distribution network. Section 4.2 discusses the pulse compression and channel estimation reflectogram processing approaches. Section 4.3 addresses the effect of the HS-OFDM-based TDR system parametrization on its performance. Finally, Section 4.4 discusses the use of multiple access schemes for power line sensing with multiple PLMs.

4.1 PROBLEM STATEMENT

In this chapter, it is assumed that an HS-OFDM system band-limited to the band $f \in [0, B]$ perfoms reflectometric sensing of the power distribution network described in Chapter 2. As the TDR system occupies a frequency bandwidth B, it is further assumed

that it has sampling frequency $F_s = 2B$. The considered HS-OFDM-based TDR system is depicted in Figure 10, starting with a complex vector $\mathbf{D} \in \mathbb{C}^{N \times 1}$. This vector is inputted to the function $\mathcal{P}(\cdot)$ that represents, in a condensed form, the digital signal processing performed at the transmitter side, which is composed by three stages. The first one is the Hermitian symmetric mapping $Map(\cdot)$ [31] that transforms $\mathbf{D}$ into the $2N$-length vector $\mathbf{X} \in \mathbb{C}^{2N \times 1}$ that represents the HS-OFDM symbol in the discrete-frequency domain. Next, the inverse discrete Fourier transform (IDFT) transforms $\mathbf{X}$ into the vector $\mathbf{x} \in \mathbb{R}^{2N \times 1} | \mathbf{x} = \frac{1}{\sqrt{2N}} \mathbf{W}_{2N}^{\dagger} \mathbf{X}$, which represents the HS-OFDM symbol in the discrete-time domain and is real-valued due to the Hermitian symmetry of $\mathbf{X}$. Finally, an L_{cp}-length cyclic prefix is appended to $\mathbf{x}$, resulting in the vector $\mathbf{s} \in \mathbb{R}^{(2N+L_{cp}) \times 1}$. Considering that the reflection channel impulse response $h_\Gamma(t)$ has a corresponding $L_{h,\Gamma}$-length discrete-time domain sequence $\{h_\Gamma[n]\}$ whose vectorial representation is $\mathbf{h}_\Gamma \in \mathbb{R}^{L_{h,\Gamma} \times 1}$, no intersymbol interference (ISI) is experienced if the constraint $L_{cp} \leq L_{h,\Gamma}$ is satisfied.

Back to Figure 10, the discrete-time vector $\mathbf{s}$ undergoes an digital-to-analog conversion, being converted into the continuous-time signal $s(t)$ that is inputted to the reflection channel of impulse response $h_\Gamma(t)$. It is worth highlighting that, in order for the LTI assumption of the reflection channel to hold, the duration of $s(t)$, i.e., the HS-OFDM symbol in the continuous-time domain, $T_{symb} = (2N + L_{cp})T_s$, must satisfy the constraint $T_{symb} \ll T_c$. The first term of the previous expression accounts for the number of samples of the discrete-time vector $\mathbf{s}$, while $T_s = 1/F_s$ is the sampling period. The resulting signal from the convolution between the transmit signal and the channel is $\tilde{r}(t) = s(t) \star h_\Gamma(t)$. To this signal is added the noise $v(t)$, which is a zero-mean WSS random process, resulting in the received signal $r(t) = s(t) \star h_\Gamma(t) + v(t)$. Note that, due to the noise presence, $r(t)$ is also a WSS random process.

At the receiver side, where perfect synchronization is assumed, the received signal $r(t)$ passes through an analog-to-digital converter, originating the vector $\mathbf{r} \in \mathbb{R}^{(2N+L_{cp}) \times 1}$. Next, $\mathbf{r}$ is inputted to the function $\mathcal{Q}(\cdot)$, which synthesizes the digital processing at the receiver side of the HS-OFDM-based TDR system. The performed processing by this function starts with cyclic prefix removal from $\mathbf{r}$, which originates the vector $\mathbf{y} \in \mathbb{R}^{2N \times 1}$.

The operations ranging from the transmitter processing on $\mathbf{x}$ to ultimately obtain $\mathbf{y}$ can be equivalently expressed as

$$\mathbf{Y} = \mathbf{X} \odot \mathbf{H}_\Gamma + \mathbf{V}, \qquad (4.1)$$

where $\mathbf{Y} \in \mathbb{C}^{2N \times 1} | \mathbf{Y} = \frac{1}{\sqrt{2N}} \mathbf{W}_{2N} \mathbf{y}$, is the discrete-frequency domain representation of $\mathbf{y}$; $\mathbf{H}_\Gamma \in \mathbb{C}^{2N \times 1} | \mathbf{H}_\Gamma = \mathbf{W}_{2N} [\mathbf{h}_\Gamma^T \mathbf{0}_{2N-L_{h,\Gamma}}]^T$ is the $2N$-length zero-padded version of $\mathbf{h}_\Gamma \in \mathbb{R}^{L_{h,\Gamma} \times 1}$; and $\mathbf{V} \in \mathbb{R}^{2N \times 1} | \mathbf{V} = \frac{1}{\sqrt{2N}} \mathbf{W}_{2N} \mathbf{v}$ is a vector composed by $2N$ Gaussian random variables and $\mathbf{v} \in \mathbb{R}^{2N \times 1}$ is a vector constituted by $2N$ consecutive samples of the discrete-time domain version of the additive noise $v(t)$.
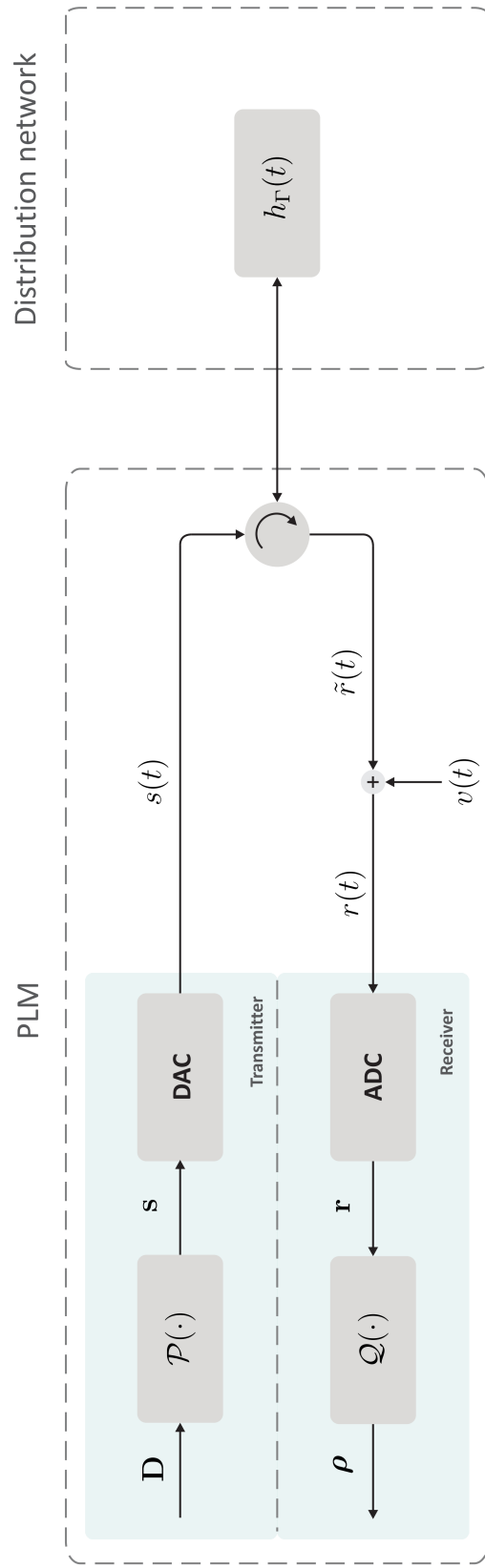
Figure 10: HS-OFDM-based TDR system over a power distribution network.

The kth element of $\mathbf{V}$, denoted by V_k, is a random variable of mean $\mathbb{E}\{V_k\} = 0$, $k \in \{0, \ldots, 2N-1\}$, and variance $\mathbb{E}\{|V_k|^2\} = \sigma_{V,k}^2$, being uncorrelated with the remaining elements of $\mathbf{V}$ in the frequency domain, i.e., $\mathbb{E}\{V_k V_j^*\} = \mathbb{E}\{V_k\}\mathbb{E}\{V_j^*\}$ for $k \in \{0, \ldots, 2N-1\}$ and $j \in \{0, \ldots, 2N-1\}$ such that $k \neq j$, $k \neq 2N - j$. Assuming that the two-sided additive noise power spectral density (PSD) is flat within each subband, one can represent it as the vector $\mathbf{S_V} \in \mathbb{R}^{2N \times 1}$, with its kth element $S_{V,k} = \sigma_{V,k}^2/(2N\Delta f)$ denoting the additive noise PSD at the kth subchannel and $\Delta f = F_s/2N$ denoting the subcarrier frequency spacing/bandwidth.

The processing performed by $\mathcal{Q}(\cdot)$ is completed with the obtaining of an L_ρ-length vector $\mathbf{P} \in \mathbb{C}^{L_\rho \times 1}|L_\rho \geq L_{h,\Gamma}$ that represents the reflectogram in the discrete-frequency domain. This is performed via processing on $\mathbf{Y}$, in such a way that the influence of $\mathbf{X}$ on it is minimized or eliminated. A proper vector $\mathbf{P}$ must be a good estimate of $\mathbf{H_\Gamma}$ and present a high SNR for noise effect to be negligible. The processing performed by $\mathcal{Q}(\cdot)$ is finally completed with a IDFT on $\mathbf{P}$, resulting in the reflectogram vector $\boldsymbol{\rho} \in \mathbb{R}^{L_\rho \times 1}$ that is actually used for analyzing the reflections along the network. Further details on $\mathbf{P}$ are provided in Section 4.2.

After the reflectogram vector $\boldsymbol{\rho}$ has been obtained, its analog counterpart $\rho(t)$ can be yielded to reduce the temporal granularity and, as a consequence, the spatial granularity of the reflectogram. This can be performed via sinc interpolation in the time domain by a reconstruction filter [54]. Alternatively, zero-padding can be performed on the discrete-frequency domain vector $\mathbf{P}$ before transforming it to the time domain [25]. Both these alternatives yield valid reflectograms under the condition that the signal has been sampled at sampling rate of at least $Fs = 2B$. A third alternative would be oversampling $r(t)$ at a sampling frequency $Fs = 2\eta B$ [30], which would ultimately yield a reflectogram vector $\boldsymbol{\rho} \in \mathbb{R}^{\eta L_\rho \times 1}|\{\eta \in \mathbb{R} \cap \eta > 1\}$, with finer temporal and spatial granularities for higher η values. Although this is a valid alternative, it would yield significantly higher computational complexity, as all processing stages at the receiver would be performed on longer vectors.

The quality of the obtained reflectogram will ultimately depend not only on the SNR level, but also on the processing performed on $\mathbf{y}$. Given this context, Section 4.2 carries out a careful description of two approaches for the obtaining of the reflectogram vector $\boldsymbol{\rho}$ from $\mathbf{y}$, which is performed by the function $\mathcal{Q}(\cdot)$.

4.2 DIGITAL REFLECTOGRAM PROCESSING APPROACHES

A conventional approach for obtaining reflectograms in TDR systems is the pulse compression, which is based on the correlation between the transmit and received signals without cyclic prefix, i.e., $\mathbf{x}$ and $\mathbf{y}$, and has already been addressed in the literature [30,55]. An alternative processing, usually resorted to in radar systems, consists of obtaining a

reflectogram vector $\boldsymbol{\rho}$ that is an adequate estimate of $\mathbf{h}_\Gamma$ by removing the effect of the transmit signal on $\mathbf{y}$ via processing in the frequency domain [56]. These two approaches are described in Subsections 4.2.1 and 4.2.2, respectively, being the digital implementation of the former approach considered rather than its analog version from Chapter 3.

4.2.1 Digital pulse compression

Similarly to Chapter 3, the digital pulse compression consists of correlating $\mathbf{y}$ with a copy of $\mathbf{x}$ so that the obtained reflectogram vector $\boldsymbol{\rho}$ is equivalent to the one obtained via the transmission of a narrower pulse, which corresponds to the autocorrelation of $\mathbf{x}$ [6, 30, 57].

Such procedure is performed via a linear convolution between the vector $\mathbf{y}$ and a matched filter to $\mathbf{x}$, denoted by $\mathbf{g} \in \mathbb{R}^{2N \times 1}$. Differently from the analog pulse compression described in Chapter 3, this linear convolution can be implemented by means of a circular convolution between $(4N - 1)$-length zero-padded versions of $\mathbf{x}$ and $\mathbf{y}$ in the digital pulse compression case, demanding computational complexity of order $\mathcal{O}(N^2)$ [54, 58]. Alternatively, it can be implemented in the discrete-frequency domain via multiplication of the $(4N - 1)$-length zero-padded versions of $\mathbf{Y}$ and $\mathbf{G} \in \mathbb{C}^{2N \times 1} | \mathbf{G} = \frac{1}{\sqrt{2N}} \mathbf{W}_{2N} \mathbf{g} = [X_0^*, X_1^*, \ldots, X_{2N-1}^*]^T$, where X_k is the kth element of $\mathbf{X}$, preceded by an discrete Fourier transform (DFT) and followed by an IDFT [55, 58]. If fast Fourier transform (FFT) and inverse fast Fourier transform (IFFT) are used, this approach becomes more efficient and faster than the circular convolution in the discrete-time domain [58], imposing the constraint that the zero-padded versions of the aforementioned vectors present length $4N$ and demanding a reduced computational complexity of order $\mathcal{O}(N \log_2 N)$.

The $4N$-length zero-padded versions of $\mathbf{Y}$ and $\mathbf{G}$ are, respecively, $\mathbf{Y}_{ZP} \in \mathbb{C}^{4N} | \mathbf{Y}_{ZP} = \frac{1}{\sqrt{4N}} \mathbf{W}_{4N} [\mathbf{y}^T \mathbf{0}_{2N}^T]^T$, and $\mathbf{G}_{ZP} \in \mathbb{C}^{4N} | \mathbf{G}_{ZP} = \frac{1}{\sqrt{4N}} \mathbf{W}_{4N} [\mathbf{g}^T \mathbf{0}_{2N}^T]^T$. The resulting reflectogram can therefore be represented in the discrete-frequency domain as

$$
\begin{aligned}
\mathbf{P}_{PC} &= \mathbf{Y}_{ZP} \odot \mathbf{G}_{ZP} \\
&= \mathbf{R}_{XX,ZP} \odot \mathbf{H}_{\Gamma,ZP} + \mathbf{V}_{ZP} \odot \mathbf{G}_{ZP},
\end{aligned}
\tag{4.2}
$$

where $\mathbf{P}_{PC}$ presents length $L_\rho = 4N$, i.e., $\mathbf{P}_{PC} \in \mathbb{C}^{4N \times 1}$; $\mathbf{R}_{XX,ZP} \in \mathbb{R}^{4N \times 1} | \mathbf{R}_{XX,ZP} = \mathbf{X}_{ZP} \odot \mathbf{G}_{ZP}$, represents the autocorrelation of $\mathbf{x}$ in the discrete-frequency domain; $\mathbf{X}_{ZP} \in \mathbb{C}^{4N} | \mathbf{X}_{ZP} = \frac{1}{\sqrt{4N}} \mathbf{W}_{4N} [\mathbf{x}^T \mathbf{0}_{2N}^T]^T$ is the $4N$-length zero-padded version of $\mathbf{X}$; $\mathbf{H}_{\Gamma,ZP} \in \mathbb{C}^{4N} | \mathbf{H}_{\Gamma,ZP} = \mathbf{W}_{4N} [\mathbf{h}_\Gamma^T \mathbf{0}_{4N-L_{h,\Gamma}}^T]^T$ is the $4N$-length zero-padded version of $\mathbf{h}_\Gamma$; and $\mathbf{V}_{ZP} \in \mathbb{C}^{4N} | \mathbf{V}_{ZP} = \frac{1}{\sqrt{4N}} \mathbf{W}_{4N} [\mathbf{v}^T \mathbf{0}_{2N}^T]^T$ represents the $4N$-length zero-padded version of $\mathbf{v}$ in the discrete-frequency domain.

A closer examination of (4.2) reveals that the obtained reflectogram is biased by the autocorrelation of the transmit signal $\mathbf{x}$. The resulting reconstructed analog reflectogram $\rho(t)$ obtained by the digital pulse-compression TDR system will be therefore equivalent to a reflectogram obtained by a conventional TDR system that performs injection of a pulse $s(t) = R_{xx}(t)$ into the network, being $R_{xx}(t)$ the continuous-time domain reconstructed version of the discrete-frequency domain autocorrelation of $\mathbf{x}$, i.e., $\mathbf{R}_{XX,ZP}$. If $R_{xx}(t)$ presents high PSLR and ISLR values [47,57], which are respectively the ratio between the highest sidelobe and the main lobe and the ratio between the integrated sidelobe level and the main lobe, there will be significant clutter, therefore compromising the quality of the reflectogram $\rho(t)$. Such distortion can be minimized by signal processing techniques such as windowing, which reduces the level of sidelobes at the cost of main lobe broadening and consequent resolution loss [30, 43, 44], or designing pulses with desired autocorrelations. The latter approach, however, may limit the use of the HS-OFDM signal to reflectometric sensing, possibly inhibiting its use for communication purposes.

4.2.2 Channel estimation

In this approach, the reflectogram $\boldsymbol{\rho}$ is obtained by performing a DFT on $\mathbf{y}$, followed by a element-wise division of the resulting vector $\mathbf{Y}$ by $\mathbf{X}$ and an IDFT [56]. The resulting operation performed by $\mathcal{Q}(\cdot)$ is therefore equivalent to a channel estimation procedure [52]. The obtained reflectogram can be expressed in the discrete-frequency domain as

$$\begin{aligned} \mathbf{P}_{CE} &= \mathbf{Y} \oslash \mathbf{X} \\ &= \mathbf{H}_\Gamma + \mathbf{V} \oslash \mathbf{X}, \end{aligned} \tag{4.3}$$

in which $\mathbf{P}_{CE} \in \mathbb{C}^{L_\rho \times 1}$ and $L_\rho = 2N$.

Finally, the reflectogram vector $\boldsymbol{\rho}$ is then simply obtained via a IDFT on $\mathbf{P}_{CE}$. If DFT and IDFT are performed by their fast counterparts, i.e., FFT and IFFT, the computational complexity associated with this procedure is of order $\mathcal{O}(N \log_2 N)$ due to the two aforementioned stages plus the Hadamard division, being therefore significantly smaller than in the digital pulse compression case. Based on the computational complexity of FFT and IFFT in the HS-OFDM scheme presented in [59], Table 1 lists the computational complexity of digital pulse compression and channel estimation reflectogram processing approaches in terms of basic operations, i.e., multiplications, divisions, sums, and subtractions.

Unlike the digital pulse compression case, the reflectogram from the channel estimation in (4.3) is only biased by noise. The only factors limiting the reflectogram quality will therefore be SNR level and system bandwidth. The band limiting of the HS-OFDM-based TDR system to a bandwidth B results in a reconstructed reflectogram $\rho(t)$ that is

Table 1: Computational complexity of digital pulse compression and chanel estimation reflectogram processing approaches.

Computational complexity			
Operations		$\times/\div$	$+/-$
Digital pulse compression	$4N$-size FFT	$8N \log_2 4N$	$12N \log_2 4N$
	Matched filtering in frequency domain	$4N$	-
	$4N$-size IFFT	$8N \log_2 4N$	$12N \log_2 4N$
Channel estimation	$2N$-size FFT	$4N \log_2 2N$	$6N \log_2 2N$
	Channel estimation in frequency domain	$2N$	-
	$2N$-size IFFT	$4N \log_2 2N$	$6N \log_2 2N$

equivalent to the one obtained by the injection of $s(t) = B\text{sinc}(Bt)$, $\text{sinc}(t) = \frac{\sin(\pi t)}{\pi t}$, into the wired network by a conventional TDR system. Although clutter level may not be as relevant as in the digital pulse compression case, it can still be reduced by windowing [60].

4.3   SYSTEM PARAMETRIZATION AND LIMITATIONS

For the HS-OFDM-based TDR system described in Section 4.1, which provides a reflectogram via digital pulse compression or channel estimation as described in Section 4.2, a proper parametrization must be performed for the resulting reflectogram to be representative of the network, besides achieving desired maximum unambiguous range and range resolution values. This is mainly done by adopting HS-OFDM symbol length $2N$, cyclic prefix length L_{cp}, and occupied frequency bandwidth B values that satisfy the aforementioned constraints, as described in the following subsections.

4.3.1   Channel coherence bandwidth

In order for $h_\Gamma(t)$ to be appropriately reconstructed from $\mathbf{h}_\Gamma$, a further constraint must be satisfied besides the one related to the channel coherence time T_c mentioned in Section 4.1. This constraint is that the frequency resolution, or subcarrier frequency spacing/bandwidth, Δf must be smaller than the reflection channel coherence bandwidth B_{c,H_Γ}, within which the reflection channel frequency response can be considered flat. The reflection channel coherence bandwidth is defined as [61]

$$B_{c,H_\Gamma} \triangleq \max_{|R_{H_\Gamma}(\Delta f)| \geq \alpha |R_{H_\Gamma}(0)|} \{\Delta f\}, \tag{4.4}$$

where $0 \leqslant \alpha \leqslant 1$ is a threshold and $R_{H_\Gamma}(\Delta f)$ is the frequency correlation function defined as by

$$R_{H_\Gamma}(\Delta f) \triangleq \int\limits_{-\infty}^{\infty} H_\Gamma(f) H_\Gamma^*(f + \Delta f) df. \qquad (4.5)$$

The frequency resolution, i.e., subcarrier frequency spacing/bandwidth, must therefore be set such that $\Delta f \leq B_{c,H_\Gamma}$. As $\Delta f = F_s/(2N)$ and $Fs = 2B$, it holds the constraint

$$N \geq \left\lceil \frac{B}{B_{c,H_\Gamma}} \right\rceil, \qquad (4.6)$$

in which $\lceil x \rceil = \min\{n \in \mathbb{Z} | n \geq x\}$.

4.3.2 Maximum unambiguous range

The maximum unambiguous range is limited by the length $2N$ of the received vector $\mathbf{y}$ [62]. This is due to the fact that, in both digital pulse compression and channel estimation, the reflectogram originates from the removal or minimization of the effect of $\mathbf{x}$ on $\mathbf{y}$. After this is done, the information on the reflection channel impulse response $h_\Gamma(t)$ will be contained in a $2N$-length vector. One must therefore have $2N \geq L_{h,\Gamma}$ so that no ambiguities to occur in the reflectogram. This holds even for the digital pulse compression case, where the reflectogram length is only longer due to zero padding.

Additionally, if the cyclic prefix is not long enough, there may be ambiguities in the reflectogram due to ISI [62]. In order to avoid such effect, the cyclic prefix length must satisfy $L_{cp} \geq L_{h,\Gamma}$. Due to the aforementioned limitations, the maximum unambiguous range in both digital pulse compression and channel estimation is given by

$$d_{\max} = \frac{v_p T_s}{2} \min\{2N, L_{cp}\}, \qquad (4.7)$$

i.e., the minimum length between $2N$ and L_{cp}, multiplied by the sampling period T_s and the phase velocity v_p and divided by 2 in order to account for the round trip time of the reflections [57]. Therefore, for a given maximum unambiguous range $d_{\max}$, one has the constraints

$$N \geq \left\lceil \frac{d_{\max}}{v_p T_s} \right\rceil \qquad (4.8)$$

and

$$L_{cp} \geq \left\lceil \frac{2d_{\max}}{v_p T_s} \right\rceil. \qquad (4.9)$$

4.3.3 Range resolution

The range resolution is the capability of resolving close reflections. For an HS-OFDM-based TDR system occupying a frequency bandwidth of B Hertz in the baseband, the corresponding range resolution is

$$\Delta d = \frac{v_p}{4B}, \qquad (4.10)$$

which, assuming perfect reconstruction of the analog reflectogram $\rho(t)$, is due to the fact that such band limiting in the frequency domain is equivalent to a convolution with a sinc with zero crossings at $\pm 1/(2B)$ in the continuous time domain as discussed in Subsection 3.3.1. The range resolution from (4.10) holds for both digital pulse compression [57, 63] and channel equalization [56] procedures.

4.4 MULTIPLE ACCESS SCHEMES

If N_{PLM} PLMs are to operate over a single power distribution network, therefore constituting a distributed HS-OFDM-based TDR system, multiple access schemes can be adopted. The most usual ones are TDMA, FDMA, and CDMA [62, 63].

For the digital pulse compression approach, TDMA, FDMA, and CDMA schemes have already been addressed in the literature [53, 63]. Out of this reason and due to the evident advantages of channel estimation over digital pulse compression pointed out in Section 4.2, the discussion on multiple access schemes for an HS-OFDM-based TDR system presented in the following subsections will assume the adoption of the channel estimation reflectogram processing approach.

Although the uth PLM, $u \in \{0, \ldots, N_{PLM} - 1\}$, is associated with an unique $\mathbf{D}_u$ vector and experiences $\mathbf{h}_{\Gamma,u}$ and $\mathbf{v}_u$ that are different for the remaining PLMs, therefore yielding an unique reflectogram vector $\boldsymbol{\rho}_u$, the subindex u will be omitted henceforth for the sake of simplicity.

4.4.1 Time-division multiple access

TDMA is a widely used multiple-input multiple-output (MIMO) scheme in applications such as radar [62] and communications [9]. For N_{PLM} PLMs transmitting and receiving $2N$-length HS-OFDM symbols, each one of them accessing the same power distribution network in different time slots, there will be no interference among reflectograms of distinct PLMs. Furthermore, each of these reflectograms will have the same maximum unambiguous range $d_{\max,TDMA} = d_{\max}$ and range resolution $\Delta d_{TDMA} = \Delta d$ exactly as defined in Section 4.3, being also subject to the channel coherence bandwidth constraint.

In this scheme, there is a number of

$$N_{\rho,TDMA} = \frac{1}{N_{PLM}T_{symb}} \tag{4.11}$$

obtained measurements per PLM per second. If intended, the PLMs that are not transmitting in the current time slot can also use the received signal from the transmitting PLM for obtaining a transferogram (i.e., channel impulse response between two PLMs), which can be used for data fusion among the PLMs [64]. This would result in a total number of $N_{meas,TDMA} = 1/T_{symb}$ measurements per PLM per second, which is constituted by

the number of reflectograms from (4.11) and

$$N_{\tau,TDMA} = \frac{N_{PLM} - 1}{N_{PLM} T_{symb}} \tag{4.12}$$

transferograms.

4.4.2 Frequency-division multiple access

In the case where different PLMs are to transmit simultaneously, an alternative is the use of the FDMA principle. For better exploiting information on the network, an interleaved FDMA scheme can be used rather than a localized one that allocated adjacent subcarriers to each PLM [30,65]. In this approach, $2N/N_{PLM}$ interleaved subcarriers are allocated to each PLM in an HS-OFDM-based TDR system with HS-OFDM symbol length $2N$. The resulting reflectogram for each PLM is therefore obtained by discarding the subcarriers allocated to the remaining PLMs and, after obtaining the vector $\mathbf{P}$, which is the vectorial representation of the reflectogram in the discrete-frequency domain, performing a $(2N/N_{PLM})$-size IDFT on it in order to obtain the reflectogram vector $\boldsymbol{\rho}$. Finally, the obtained $(2N/N_{PLM})$-length reflectogram $\boldsymbol{\rho}$ undergoes a reconstruction process that will originate $\rho(t)$ as described in Section 4.1.

In the considered FDMA scheme, the vector $\mathbf{D} \in \mathbb{C}^{N \times 1}$, from Section 4.1 is generated via a pre-mapping on a vector $\dot{\mathbf{D}} \in \mathbb{C}^{(N+1) \times 1}$, whose k^{th} element $\dot{D}_k$ will be ultimately transmitted at the continuous-frequency bin $f_k = k\Delta f$ Hz after all processing and digital-to-analog conversion has been performed at the transmitter side. This pre-mapping is expressed as

$$D_k = \begin{cases} \dot{D}_{k+1}, & k = 0, \ldots, N-2 \\ \dot{D}_0 + j\dot{D}_N, & k = N-1 \end{cases}, \tag{4.13}$$

where D_k is the kth element of $\mathbf{D}$, and $j = \sqrt{-1}$. In order for interference-free operation of the PLMs to take place, a set $\mathcal{K}_u = \{u, u + N_{PLM}, u + 2N_{PLM}, \ldots\}$, $u \in \{0, \ldots, N_{PLM} - 1\}$, of N/N_{PLM} interleaved elements of $\dot{\mathbf{D}}$ are allocated to the uth PLM. Also, all PLMs place null values at the elements that have not been allocated to it.

Once $\mathbf{P}$ has been obtained at the receiver side, the PLM performs a channel estimation processing considering only its elements associated with the ones of $\dot{\mathbf{D}}$ whose indexes belong to $\mathcal{K}_u$. Next, $\mathbf{P}$ is transformed into the vector $\dot{\mathbf{P}} \in \mathbb{R}^{(N+1) \times 1}$ according to the mapping

$$\dot{P}_k = \begin{cases} P_k, & k = 0, N \\ 2P_k, & k = 1, \ldots, N-1 \end{cases}, \tag{4.14}$$

in which P_k and $\dot{P}_k$ are the kth elements of $\mathbf{P}$ and $\dot{P}_k$, respectively. Such mapping is performed in order to map a $2N$-length Hermitian symmertric vector $\mathbf{P}$ into the N-length vector $\dot{\mathbf{P}}$ with no loss of spectral content.

Finally, the uth PLM obtains an L_ρ-length reflectogram vector $\boldsymbol{\rho} \in \mathbb{R}^{L_\rho \times 1}$, $L_\rho = 2N/N_{PLM}$, whose n^{th} element is expressed as

$$
\begin{aligned}
\rho_n \;=\; & \frac{1}{\sqrt{L_\rho}} \left[\sum_{k \in \mathcal{K}_u} \Re\{\dot{P}_k\} \cos\left(\frac{\pi k n}{N}\right) \right. \\
& \left. - \sum_{k \in \mathcal{K}_u} \Im\{\dot{P}_k\} \sin\left(\frac{\pi k n}{N}\right) \right],
\end{aligned}
\tag{4.15}
$$

which, for the single-PLM case, is exactly the same result obtained by performing an IDFT on $\mathbf{P}$.

The obtained reflectograms in the proposed FDMA scheme will have maximum unambiguous range experienced by each PLM equal to $d_{\max,FDMA} = d_{\max}/N_{PLM}$. The range resolution for each PLM in its turn will be $\Delta d FDMA = v_p/(4 B_{FDMA})$, with B_{FDMA} being the effective bandwidth experienced by each PLM. As $2N/N_{PLM}$ subcarriers are allocated to each PLM, the effective subcarrier separation experienced by the latter will be $\Delta f_{FDMA} = (N_{PLM}/N)B$. Consequently, $B_{FDMA} = (N/N_{PLM})\Delta f_{FDMA} = B$, and it holds that the range resolution is exactly as defined in Section 4.3 for the single-user case, i.e., $\Delta d FDMA = \Delta d$. Although the range resolution is maintained, the information on the network contained in the subcarriers discarded by the PLM will cause distortion on the obtained reflectograms. The trade-off between number of PLMs connected to the network and reflectogram quality must therefore be observed in order for fault detection and location procedures not to be negatively affected.

As a consequence, one obtains a number of

$$
N_{\rho,FDMA} = \frac{1}{T_{symb}}
\tag{4.16}
$$

reflectograms per PLM per second. If transferograms are also to be obtained, one would have a total number of $N_{meas,FDMA} = N_{PLM}/T_{symb}$ measurements per PLM per second, encompassing the number of reflectograms from (4.16) and

$$
N_{\tau,FDMA} = \frac{N_{PLM} - 1}{T_{symb}}
\tag{4.17}
$$

transferograms.

4.4.3 Code-division multiple access

Unlike TDMA and FDMA schemes, the use of CDMA allows the PLMs to occupy the entire bandwidth over all time slots [53, 62, 63]. The implementation of this scheme consists of adding an encoding process on the vector $\mathbf{D}$.

In this context, let us consider an N_{PLM}-size Hadamard matrix whose rows are constituted by codewords that are orthogonal among each other. The codeword of the uth row of this matrix is represented by the vector $\mathbf{C}_u \in \{-1, 1\}^{N_{PLM} \times 1}$, which is, in its turn, allocated to the uth PLM. Due to the existing orthogonality among the codewords, the mutual interference among the PLMs is minimized.

The encoding process performed by the uth PLM is then performed via a multiplication between the codeword vector by the transpose counterpart of $\mathbf{D} \in \mathbb{C}^{N \times 1}$, resulting in the spread symbol matrix

$$\mathbf{D}_{C,u} = \mathbf{C}_u \mathbf{D}^T, \tag{4.18}$$

for which holds $\mathbf{D}_{C,u} \in \mathbb{C}^{N_{PLM} \times N}$. The N_{PLM} rows of this matrix are then sequentially fed to the Hermitian symmetric mapping and further processing, being finally transmitted by the uth PLM. Thus, the necessary time for transmitting the vector $\mathbf{D}$ is N_{PLM} times longer than the T_{symb} seconds of the single-PLM case.

After cyclic prefix removal and DFT are performed on the N_{PLM} received symbols at the receiver side, a reception matrix $\mathbf{Y}_C \in \mathbb{C}^{N_{PLM} \times 2N}$ is formed, being its rows associated with the rows of $\mathbf{D}_{C,u}$.

$$\mathbf{Y}_C = \mathbf{X}_C \odot \mathbf{H}_{\Gamma,C} + \mathbf{V}_C + \mathbf{V}_{C,I}, \tag{4.19}$$

where $\mathbf{X}_C \in \mathbb{C}^{N_{PLM} \times 2N}$ is a transmission matrix whose rows result from the Hermitian symmetric mapping on the respective rows of $\mathbf{D}_{C,u}$; $\mathbf{H}_{\Gamma,C} \in \mathbb{C}^{N_{PLM} \times 2N}$ is an equivalent reflection channel matrix, expressed as $\mathbf{H}_{\Gamma,C} = \mathbf{1}_{N_{PLM} \times 1} \mathbf{H}_\Gamma^T$; $\mathbf{V} \in \mathbb{C}^{N_{PLM} \times 2N}$ is a noise matrix whose rows are constituted by $2N$ consecutive samples of the additive noise $v(t)$ in the discrete-frequency domain; and $\mathbf{V}_I$ is the interference noise matrix, which accounts for the mutual interference among the PLMs. The uth PLM then performs a decoding process on $\mathbf{Y}_C$, which generates the vector $\mathbf{Y} \in \mathbb{C}^{2N \times 1}$ and is expressed as

$$\mathbf{Y} = \frac{\left(\mathbf{C}_u^T \mathbf{Y}_C\right)^T}{\mathbf{card}\{\mathbf{C}_u\}}, \tag{4.20}$$

where $\mathbf{card}\{\cdot\}$ is a function that returns the cardinality of an inputted vector. The vector $\mathbf{Y}$ can be alternatively expressed as

$$\mathbf{Y} = \mathbf{X} \odot \mathbf{H}_\Gamma + \hat{\mathbf{V}} + \hat{\mathbf{V}}_I, \tag{4.21}$$

in which $\hat{\mathbf{V}} = \left(\mathbf{C}_u^T \mathbf{V}_C\right)^T / \mathbf{card}\{\mathbf{C}_u\}$ is the resulting additive noise from the decoding process, whose PSD is expressed as $\mathbf{S}_{\hat{\mathbf{V}}} \in \mathbb{R}^{2N \times 1}$, with $S_{\hat{V},k} = (\sigma_{V,k}^2 / \sqrt{N_{PLM}})/(2N\Delta f)$ representing the resulting additive noise PSD at the kth subchannel; and $\hat{\mathbf{V}}_I = \left(\mathbf{C}_u^T \mathbf{V}_{C,I}\right)^T / |\mathbf{C}_u|$ is the resulting interference noise. The fact that the resulting additive noise PSD is $\sqrt{N_{PLM}}$ times smaller than the one of the original additive noise $\mathbf{V}$ is due to the averaging process that happens at the decoding stage of the CDMA scheme in (4.20) and ultimately results in an SNR gain [53].

Instead of the digital pulse compression from [53], channel estimation is performed on $\mathbf{Y}$ after this stage as described in Subsection 4.2.2 for the single-PLM case. The resulting vector $\mathbf{P}$ finally undergoes an IDFT, originating the reflectogram vector $\boldsymbol{\rho}$. Although the effect of the transmit symbol on the reflectogram is properly removed, the use of CDMA introduces mutual interference among the PLMs, whose reflectograms consist of the reflections raised by the injected signal by the own PLM plus a term that accounts for the decoded symbols transmitted by the remaining PLMs as well as additive noise. Despite being significantly attenuated by the decoding process, this interference term might distort the obtained reflectogram [62].

In spite of the undesired interference, the obtained reflectograms in the CDMA scheme yield the same maximum unambiguous range $d_{\mathrm{max},CDMA} = d_{\mathrm{max}}$ and range resolution $\Delta d CDMA = \Delta d$ as in the single-user case from Section 4.3, whose channel coherence bandwidth constraint still holds. Due to the extended transmission time, a number

$$N_{\rho,CDMA} = \frac{1}{N_{PLM}T_{symb}} \tag{4.22}$$

of reflectograms are obtained per PLM per second. In the case where transferograms are also obtained, the total number of measurements per PLM per second would be $N_{meas,CDMA} = 1/T_{symb}$ measurements, which encompasses the number of reflectograms from (4.22) and

$$N_{\tau,CDMA} = \frac{N_{PLM} - 1}{N_{PLM}T_{symb}} \tag{4.23}$$

transferograms.

5 ORTHOGONAL CHIRP-DIVISION MULTIPLEXING FOR POWER LINE SENSING VIA TDR

Multicarrier-based TDR systems allow effective digital reflectogram processing while also enabling simplified spectrum managing for complying to EMC constraints. A variation of one of such systems, the OMTDR, which was originally considered for wiring network scenarios such as aircraft, has been discussed in Chapter 4, where the channel estimation procedure was introduced as an alternative to pulse compression.

For improved network sensing, such TDR systems based on multicarrier schemes can constitute a distributed sensing system of the monitored power distribution network. Aiming such purpose, research efforts have already been done for multicarrier-based TDR systems [53]. Also, multiple access schemes based on TDMA, FDMA, and CDMA, have been discussed for TDR systems based on HS-OFDM in Chapter 4. While the use of TDMA requires a complex clock synchronization scheme among the PLMs that constitute the distributed sensing system and jeopardizes the sensing of e.g. intermittent changes in the power line, the use of FDMA may result in loss of spectral content in the obtained reflectograms and transferograms. Despite having better sensibility to changes in the power line than TDMA and not losing spectral content of the measurements as in the FDMA case, the use of CDMA results in the obtaining of a small number of measurements over time due to the spreading of its transmit signal.

Recently, OCDM, which is a multicarrier scheme based on the DFnT, has been proposed for wireless systems [66]. Such scheme has shown robustness to multipath propagation, being an interesting alternative for digital data communication. Furthermore, four modified versions of DFnT that allow the extension of such scheme for baseband data transmission in PLC systems have been proposed [34]. One of these four versions, named Type III OCDM in [34], adds Hermitian symmetry to the DFnT matrix in order to produce a real-valued transmit vector in the discrete-time domain demanding low computational complexity.

Considering the modified DFnT of the Type III OCDM from [34], this chapter describes an OCDM-based TDR system for power line sensing. Based on the convolution theorem of the DFnT, which also holds for the modified DFnT, a multiple access scheme is then introduced for the OCDM-based TDR system. The remainder of this chapter is organized as follows. The OCDM-based TDR system for sensing of a power distribution network is described in Section 5.1 considering the single PLM case. Next, Section 5.2 discusses range resolution and maximum unambiguous range aspects of the considered TDR system and introduces a novel multiple access scheme based on OCDM.

5.1 PROBLEM STATEMENT

Similarly to Chapter 4, a multicarrier TDR system system occupying a frequency band denoted by $f \in [0, B]$, therefore having frequency bandwidth B, is considered to perform reflectometric power line sensing of the scenario described in Chapter 2. Also, a sampling frequency $F_s = 2B$ is adopted. In Figure 11, the real-valued vector $\dot{\mathbf{x}} \in \mathbb{R}^{2N \times 1}$ that represents the OCDM symbol in the discrete-Fresnel domain is inputted to the function $\mathcal{P}(\cdot)$ that represents, in a condensed form, the twofold digital processing performed at the transmitter side of the OCDM-based TDR system. Such processing performed by $\mathcal{P}(\cdot)$ starts with a modified inverse discrete Fresnel transform (IDFnT) on $\dot{\mathbf{x}}$, resulting in the $2N$-length vector $\mathbf{x} \in \mathbb{R}^{2N \times 1} | \mathbf{x} = \mathbf{\Phi}_{2N}^{\dagger} \dot{\mathbf{x}}$ that represents the OCDM symbol in the discrete-time domain. Next, an L_{cp}-length cyclic prefix is finally appended to $\mathbf{x}$, originating the vector $\mathbf{s} \in \mathbb{R}^{(2N+L_{cp}) \times 1}$. If ISI is to be avoided, one must satisfy the constraint $L_{cp} \leq L_{h,\Gamma}$, where $L_{h,\Gamma}$ is the length of the discrete-time domain sequence $\{h_{\Gamma}[n]\}$ associated with the reflection channel impulse response $h_{\Gamma}(t)$, whose vectorial representation is $\mathbf{h}_{\Gamma} \in \mathbb{R}^{L_{h,\Gamma} \times 1}$.

Still at the transmitter side of the OCDM-based TDR system, the vector $\mathbf{s}$ is transformed into the continuous-time signal $s(t)$ via digital-to-analog conversion as shown in Figure 11. The signal $s(t)$ is then injected into the power distribution network whose reflection channel of impulse response is $h_{\Gamma}(t)$. As in Chapter 4, the reflection channel can only be assumed to be LTI if the duration T_{symb} of the transmit signal $s(t)$, which represents the OCDM symbol in the continuous-time domain, satisfies the constraint $T_{\text{symb}} \ll T_c$. Considering a sampling period $T_s = 1/F_s$, the OCDM symbol duration is $T_{\text{symb}} = (2N + L_{cp})T_s$. The outputted signal from the reflection channel is then $\tilde{r}(t) = s(t) \star h_{\Gamma}(t)$, to which is added the noise $v(t)$. Due to the fact that $v(t)$ is a zero-mean WSS random process, the ultimately received signal $r(t) = s(t) \star h_{\Gamma}(t) + v(t)$ is also a WSS random process.

The processing performed at the receiver side is preceded by an analog-to-digital conversion on the received signal $r(t)$. This ultimately results in the vector $\mathbf{r} \in \mathbb{R}^{(2N+L_{cp}) \times 1}$, which is then inputted to the function $\mathcal{Q}(\cdot)$ that synthesizes the digital signal processing at the receiver side of the OCDM-based TDR system. First, $\mathcal{Q}(\cdot)$ removes the cyclic prefix from $\mathbf{r}$, originating the vector $\mathbf{y} \in \mathbb{R}^{2N \times 1}$ that is expressed as

$$\mathbf{y} = \mathbf{H}_{\Gamma}\mathbf{x} + \mathbf{v}, \tag{5.1}$$

where $\mathbf{H}_{\Gamma} \in \mathbb{R}^{2N \times 2N}$ is a circulant matrix associated with a zero-padded version of $\mathbf{h}_{\Gamma}$, and $\mathbf{v} \in \mathbb{R}^{2N \times 1}$ is a $2N$-length vector constituted by $2N$ consecutive samples of the discrete-time domain version of the additive noise $v(t)$. Next, a modified DFnT is performed on $\mathbf{y}$, which results in the vector $\dot{\mathbf{y}} \in \mathbb{R}^{2N \times 1}$. As the convolution theorem of the DFnT also holds for the modified DFnT, which is demonstrated in the Appendix A, $\dot{\mathbf{y}}$ can be equivalently

expressed as

$$\dot{\mathbf{y}} = \mathbf{H}_\Gamma \dot{\mathbf{x}} + \dot{\mathbf{v}}, \tag{5.2}$$

being $\dot{\mathbf{v}} \in \mathbb{R}^{2N \times 1}$ a $2N$-length vector obtained by performing a DFnT on $\mathbf{v}$.
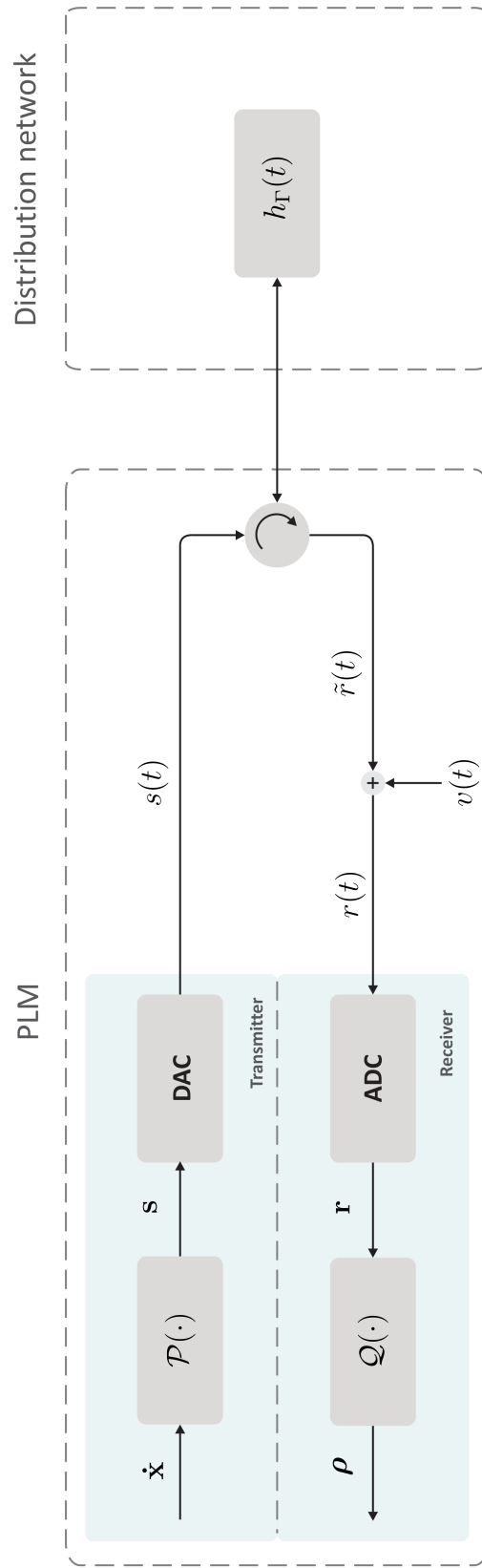
Figure 11: OCDM-based baseband TDR system over a distribution network.

The last stage of the digital signal processing performed by $\mathcal{Q}(\cdot)$ is the obtaining of an L_ρ-length reflectogram vector, denoted as $\boldsymbol{\rho} \in \mathbb{R}^{L_\rho \times 1} | \{L_\rho \in \mathbb{N}^* \cap L_\rho \geq L_{h,\Gamma}\}$, from $\dot{\mathbf{y}}$. Besides ensuring high SNR in order for noise effect to be negligible, a proper reflectogram must have the influence of $\dot{\mathbf{x}}$ on it minimized or eliminated so that a good estimate of $\mathbf{h}_\Gamma$ is obtained. In this study, this is accomplished by simply designing a proper vector $\dot{\mathbf{x}}$ so that $\boldsymbol{\rho}$ is directly obtained from $\dot{\mathbf{y}}$ with no additional processing. Also, for covering cases where multiple PLMs are to perform network sensing simultaneously, this design must also enable orthogonal multiple access among the PLMs. A discussion on the design of $\dot{\mathbf{x}}$ is presented in Section 5.2.

As discussed in Chapter 4, temporal and therefore spatial granularity reduction of the discrete-time domain reflectogram $\boldsymbol{\rho}$ can be yielded by means of reconstruction of the continuous-time domain reflectogram $\rho(t)$. In the case of the OCDM-based TDR system, an interesting approach would be sinc interpolation in the time domain by a reconstruction filter [54] as the reflectogram is obtained in the discrete-Fresnel domain and interpreted as if it were in the discrete-time domain.

5.2   DISTRIBUTED POWER LINE SENSING

As discussed in Section 5.1, for obtaining a proper reflectogram from $\dot{\mathbf{y}}$, the influence of $\dot{\mathbf{x}}$ on it, as expressed in (5.2), must be minimized or ideally removed. Considering that a single PLM performs sensing of the power distribution network, a vector $\dot{\mathbf{x}}$ constituted of pilots spaced by L_ρ elements can be used [67, 68]. Thus, the kth element of $\dot{\mathbf{x}}$ will be given by

$$\dot{x}_k = \sum_{u=0}^{2N/L_\rho - 1} \delta[k - uL_\rho],$$

(5.3)

in which $k \in \{0, \ldots, 2N - 1\}$. Based on the convolution theorem of the modified DFnT, the kth element of the resulting vector $\dot{\mathbf{y}}$ can be expressed as

$$\dot{y}_k = \left(\sum_{u=0}^{2N/L_\rho - 1} h_{\Gamma, k - uL_\rho} \right) + \dot{v}_k,$$

(5.4)

where $h_{\Gamma,k}$ and $\dot{v}_k$ denote the kth elements of vectors $\mathbf{h}_\Gamma$ and $\dot{\mathbf{v}}$, respectively. Note that $h_{\Gamma, k - uL_\rho} = 0$ for $k - uL_\rho < 0$ and $k - uL_\rho > L_{h,\Gamma} - 1$, as $h_{\Gamma,k}$ is only defined for $k \in \{0, \ldots, L_{h,\Gamma} - 1\}$. As a consequence, $\dot{\mathbf{y}}$ will be constituted of concatenated estimates of the reflection channel impulse response impaired by additive noise, which will not cause mutual interference on each other if the spacing between consecutive pilots is equal to or longer than the length of $\mathbf{h}_\Gamma$, i.e., $L_\rho \geq L_{h,\Gamma}$. Finally, $2N/L_\rho$ unbiased discrete-time domain reflectograms are obtained by dividing the vector $\dot{\mathbf{y}}$ into L_ρ-length windows. Consequently, such channel estimation is equivalent to an ideal pulse compression, whose capability of distinguishing reflections caused by close impedance discontinuities, i.e., range

resolution, is given by [57, 69]

$$\Delta d = \frac{v_p}{4B}. \tag{5.5}$$

The range resolution in the OCDM-based TDR system is therefore the same from (4.10), being defined by the frequency bandwidth to which the system is constrained. Additionally, the PSLR and ISLR levels of each obtained estimate will only depend upon the occupied frequency bandwidth B in the baseband by the TDR system as described in Chapter 4.

In the proposed OCDM-based TDR system, the maximum unambiguous range is limited by both the measurement window length L_ρ and the cyclic prefix length L_{cp}. As previously discussed, L_ρ must be set so that there is no mutual interference among measurement windows. L_{cp}, in its turn, must be long enough so that no ISI is experienced. Based on the discussion carried out in Chapter 4, the maximum unambiguous range for reflectograms is

$$d_{\max,\rho} = \frac{v_p T_s}{2} \min\{L_\rho, L_{cp}\}. \tag{5.6}$$

For transferograms, the maximum unambiguous range is

$$d_{\max,\tau} = v_p T_s \min\{L_\rho, L_{cp}\}, \tag{5.7}$$

which is twice the value assumed by $d_{\max,r}$, in which the round trip time for the transmitted travelling waves is considered.

Moving to the case where N_{PLM} PLMs perform sensing of a single power distribution network simultaneously, an efficient multiple access strategy must be adopted. In the case of HS-OFDM-based TDR systems, TDMA, FDMA, and CDMA schemes have been discussed in Chapter 4. For the case of the OCDM-based TDR system considered in this study, the orthogonality among the signals associated with the multiple PLMs is ensured by a proper subchirp allocation among them.

The proposed subchirp allocation scheme for enabling multiple access among PLMs performing unbiased power line sensing is shown in Fig. 12. In this figure, the subchirp pilot of index $k = uL_\rho$ of the $2N$-length vector $\dot{\mathbf{x}}$ is active for the uth PLM, $u \in \{0, \dots, N_{PLM} - 1\}$. For the sake of fairness, the distance between the element associated with the active pilot of the uth PLM and the element associated with the active pilot of the $(u + 1)^{th}$ PLM is set to $L_\rho = 2N/N_{PLM}$.

At the receiver side, the vector $\dot{\mathbf{y}}$ at the uth PLM will be composed of N_{PLM} measurement windows. The uth measurement window starts at the subchirp $k = uL_\rho$ and ends at the subchirp $k = uL_\rho + L_\rho - 1$ of $\dot{\mathbf{y}}$ and it is a reflectogram at the uth PLM and a transferogram at the remaining PLMs. In order to perform effective power line sensing, data fusion techniques can be applied on the obtained measurement windows [64].
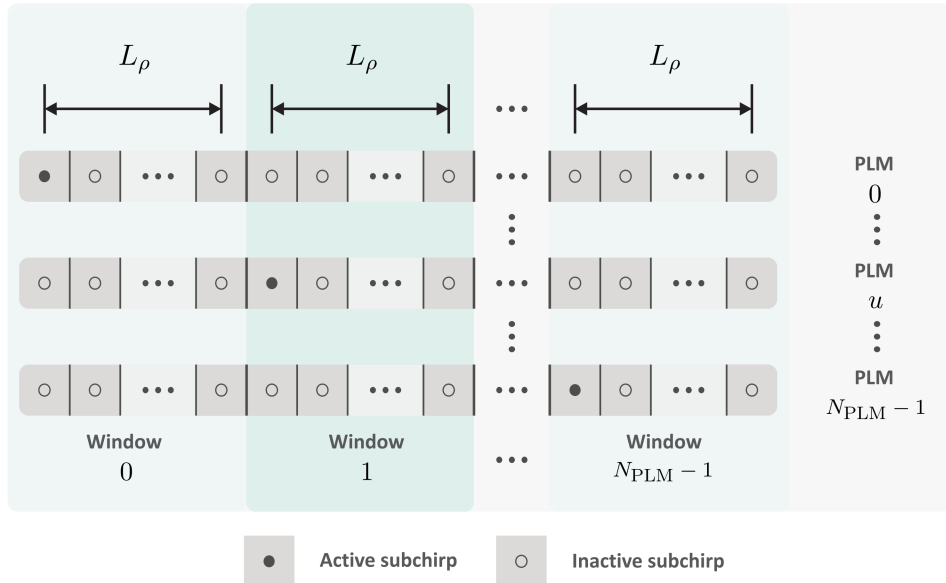
Figure 12: Subchirp allocation among the PLMs.

In order to avoid interference among measurement windows, the spacing among pilots must satisfy the constraint $L_\rho = 2N/N_{PLM} \geq L_{h,\max}$, or alternatively

$$2N \geq N_{PLM} L_{h,\max}. \tag{5.8}$$

For this constraint, $L_{h,\max}$ is defined as

$$L_{h,\max} \triangleq \max_{ij}\{L_{h,ij}\}, \tag{5.9}$$

where $L_{h,ij}$ is the length of the channel impulse response $\mathbf{h}_{ij} \in \mathbb{R}^{L_{h,ij} \times 1}$ for a signal injected by the jth PLM into the power distribution network and received by the ith PLM, with $i \in \{0, \ldots, N_{PLM} - 1\}$ and $j \in \{0, \ldots, N_{PLM} - 1\}$. Altogether, there are N_{PLM}^2 channel impulse responses $\mathbf{h}_{ij}$, with a total of N_{PLM} reflectograms ($\mathbf{h}_{ij}$, $i = j$) and $N_{PLM}(N_{PLM} - 1)$ transferograms ($\mathbf{h}_{ij}$, $i \neq j$).

The proposed multiple access scheme and OCDM-based TDR system parametrization result in the obtaining of a number

$$N_{\rho,OCDM} = \frac{1}{T_{symb}} \tag{5.10}$$

reflectograms per PLM per second. Additionally,

$$N_{\tau,OCDM} = \frac{N_{PLM} - 1}{T_{symb}} \tag{5.11}$$

transferograms are obtained per PLM per second, resulting in a total number of $N_{meas,OCDM} = N_{\rho,OCDM} + N_{\tau,OCDM} = N_{PLM}/T_{symb}$ measurements per PLM per second.

6 NUMERICAL RESULTS

In this chapter, numerical results are presented for supporting the carried out discussion in Chapters 3, 4, and 5. In the analog reflectogram processing context of Chapter 3, Section 6.1 performs a comparative analysis among the HS-OFDM, UWB (first and second derivatives of the Gaussian pulse), and CSS PLC pulses, covering typical European underground low voltage (LV) and US overhead medium voltage (MV) scenarios and using range resolution, PCR, PSLR, ISLR, and maximum unambiguous range as performance metrics. Also, results for PLC-based pulse-compression TDR systems complying with narrowband (NB)- and broadband (BB)-PLC regulations are presented and discussed.

Next, a discussion on the multicarrier TDR systems based on HS-OFDM and OCDM schemes described in Chapters 4 and 5 is carried out in Section 6.2. After comparing digital pulse compression and channel estimation reflectogram processing approaches of the HS-OFDM scheme to support the latter, the same LV and MV scenarios from Section 6.1 are considered for assessing the performance in terms of range resolution and maximum unambiguous range of both HS-OFDM- and OCDM-based TDR systems. Finally, TDMA, FDMA, and CDMA multiple access schemes based on HS-OFDM are compared with the proposed OCDM-based multiple access scheme in terms of number of measurements over time and SINR, being a Brazilian overhead MV scenario considered for the latter analysis.

6.1 COMPARISON OF TYPICAL PLC PULSES FOR POWER LINE SENSING VIA TDR

In order to investigate the characteristics of the four considered PLC pulses for power line sensing via TDR, this section assesses their performance in terms of the aspects of range resolution, PCR, reflectogram distortion, and maximum unambiguous range. Two scenarios are considered for this purpose, namely an European underground low-voltage power distribution network and an US overhead medium-voltage power distribution network in a rural area. For the low-voltage scenario, a power supply cable NAYY150SE with resistance R', inductance L', conductance G', and capacitance C' per unit length calculated as in [70] is considered, whereas for the medium-voltage cable, the power supply cable with distributed parameters listed in [71] is adopted. These parameters, as well as their associated phase velocity, which is calculated by $v_p = 1/\sqrt{L'C'}$ [5], are listed in Table 2.

Due to frequency bandwidth occupancy limitations, which belong to EMC constraints imposed by regulations, the influence of the pulse duration T on the occupied frequency bandwidth B is first analyzed. Figures 13a and 13b show B versus T curves for

Table 2: Per unit length parameters and phase velocity of the considered cables.

Scenario	Resistance R' (Ω/m)	Inductance L'(μH/m)	Conductance G' (μS/m)	Capacitance C' (pF/m)	Phase velocity v_p (m/s)
LV	$21.31 \times 10^{-}6$	0.14	9.64	306.95	1.50×10^8
MV	0.03	1.90	1.50	8.00	2.56×10^8

the four considered PLC pulses for NB-PLC and BB-PLC, respectively. In these figures, the curves for the UWB pulses show very similar behavior with much steeper decay than the curves for HS-OFDM and CSS pulses, which is due to their pulse-shaped nature. For the carried out analysis in this subsection, a number of $N = 512$ subcarriers is adopted for the HS-OFDM scheme and equal duration for HS-OFDM and CSS pulses for a given frequency bandwidth is considered, which implies in increasing μ along with B. This is justified by the fact that CSS pulses would present far longer T for high B values if a fixed μ value is adopted and it results in increasing implementation complexity along with B, as larger frequency bandwidths must be swept in shorter time intervals. The observed μ values, however, are up to 0.98 kHz/μs for NB-PLC, and up to 28.89 MHz/μs for BB-PLC systems, which is considerably smaller than what is reported for applications such as radar [72] and therefore indicates the feasibility of the presented μ and B pairs.

The second aspect of our analysis is based on range resolution and PCR, being the former shown in Figures 14a and 14b as a function of T for all four PLC pulses for NB- and BB-PLC systems and the latter in Table 3, respectively. In these figures, the left vertical axes show the range resolution Δd_{LV} for the considered low-voltage power distribution network, while the vertical axes on the right side shows range resolution Δd_{MV} for the considered medium-voltage power distribution network. Once again the UWB pulses present very similar behavior, with the first and second derivatives of the Gaussian pulse presenting low PCR, i.e., $PCR_{UWB-1} = 4.95$ and $PCR_{UWB-2} = 6.67$, respectively. In this analysis, the finest resolution, i.e., the best capability of resolving two close impedance discontinuities, is achieved by HS-OFDM and CSS pulses. With the chosen parameters, these pulses present the highest PCRs, which are $PCR_{HS-OFDM} = PCR_{CSS} = 1024$. For NB, the achieved range resolution values range from a few meters for short pulses to tens of thousands of kilometers for longer pulses, with a ratio of 1.71 between the resolution in the MV and LV and scenarios due to their different phase velocity. BB pulses, on the other hand, yield range resolution values from a few millimeters for short pulses to a few meters for longer pulses with the same ratio between MV and LV cases. As PLC signaling in LV and MV power distribution networks may cover lengths of hundreds of meters [73] and units to tens of kilometers [71], respectively, the presented results indicate that NB
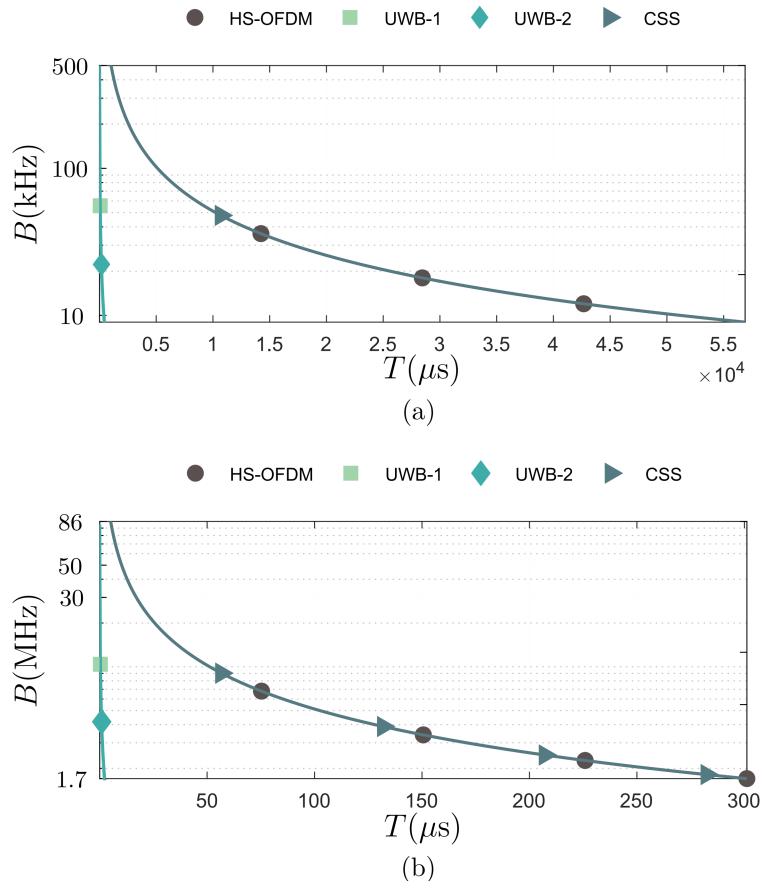
Figure 13: Occupied frequency bandwidth B as a function of the pulse duration T for (a) NB-PLC and (b) BB-PLC systems.

pulses provide a fair capability of resolving close impedance discontinuities in most cases, being the most suitable option for most distribution network scenarios. The use of BB pulses is therefore limited to cases where a very fine resolution is desired, such as very short sections of distribution networks.

A further topic of our analysis is the comparison among the four considered PLC pulses in terms of PSLR and ISLR, whose values are shown in Table 4. In this table, one sees that UWB pulses present the worst performances in terms of PSLR, being outperformed by the HS-OFDM pulse. The CSS pulse yields the best PSLR value, which is somewhat lower than the 13.2 dB reported in the literature for bandpass chirps in radar applications. In terms of ISLR, however, the performance ranking is altered. The first derivative of the Gaussian pulse presents the best ISLR, followed by CSS pulse, the second derivative of the Gaussian pulse and the HS-OFDM pulse, in this order. Such result is explained by the fact that, disregarding the sidelobes surrounding the main lobe, $R_{pp,UWB-1}(\tau)$ presents insignificant sidelobe level, as seen in Figure 6b. This, however, does not hold for $R_{pp,UWB-2}(\tau)$, as seen in Figure 7b. The relevant ISLR for the HS-OFDM and CSS pulses in comparison to the obtained value for the second derivative of the Gaussian pulse is explained by their higher PCR. As a matter of fact, the sidelobe
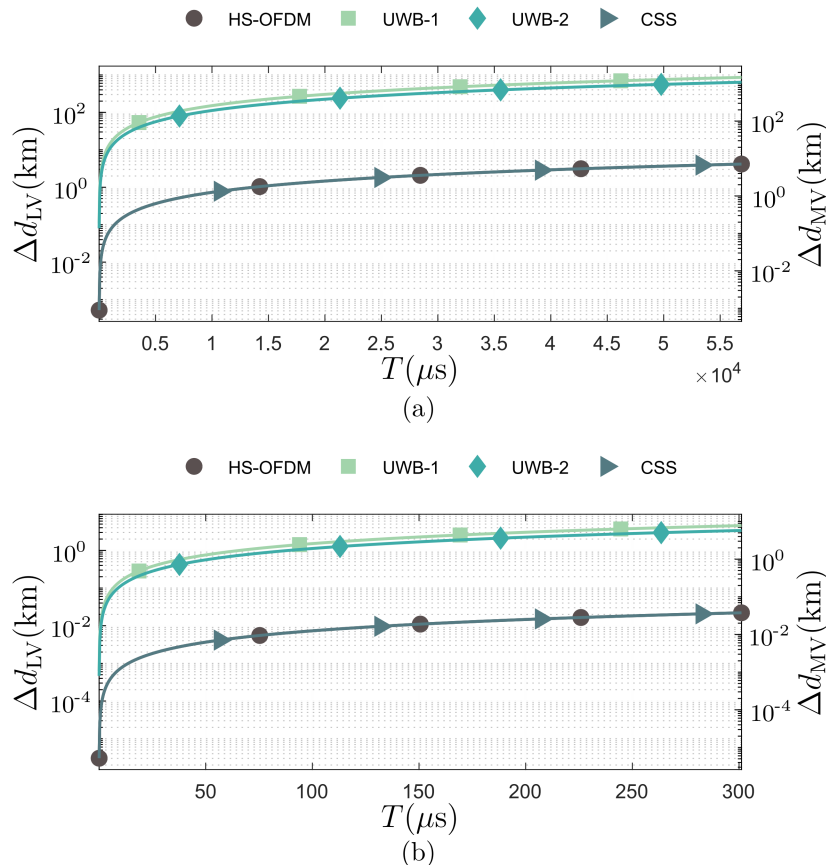
Figure 14: Range resolution Δd_{LV} and Δd_{MV} for respectively LV and MV scenarios as a function of the pulse duration T for (a) NB-PLC and (b) BB-PLC systems.

Table 3: PCR for the considered PLC pulses.

Pulse	PCR
HS-OFDM	1024
UWB-1	4.95
UWB-2	6.67
CSS	1024

level of both $R_{pp,OFDM}(\tau)$ and $R_{pp,CS}(\tau)$ is not negligible even at the extremities and their main lobes are very narrow and, as a consequence, the ratio between them yields an expressive value. Finally, it is worth emphasizing that, in the HS-OFDM case, better results may be achieved via appropriate pulse design with more robust techniques such as in [47, 74].

Next, the maximum unambiguous range values achieved by the four PLC pulses are shown in Figures 15a and 15b for NB- and BB-PLC, respectively. In these figures, the left vertical axis shows $d_{\mathrm{max,LV}}$ for the considered low-voltage power distribution network, whereas the vertical axis on the right side shows $d_{\mathrm{max,MV}}$ for the considered medium-voltage power distribution network. Also, pulse repetition intervals of $\Delta T_p = 0.01\mathrm{ms}$,

Table 4: ISLR and PSLR for the considered PLC pulses.

Pulse	PSLR	ISLR
HS-OFDM	-13.42dB	-0.67dB
UWB-1	-7.01dB	-3.77dB
UWB-2	-4.18dB	-0.94dB
CSS	-14.04dB	-1.75dB

$\Delta T_p = 0.1$ms, $\Delta T_p = 1$ms, and $\Delta T_p = 10$ms were adopted. In these figures, one sees that longer pulses result in a shorter maximum unambiguous range for a given pulse interval rate, as one can easily conclude by analyzing (3.32). In this sense, NB pulses present shorter maximum unambiguous range values than BB pulses due to their longer duration, which is clear through a comparison of Figures 15a and 15b. We also see that pulse repetition intervals of $\Delta T_p = 1$ms and $\Delta T_p = 0.01$ms cover typical MV and LV distances for NB pulses for T values associated with great part of the NB frequency range, while ΔT_p of a few unities of milliseconds are necessary to cover both MV and LV scenarios for BB pulses.
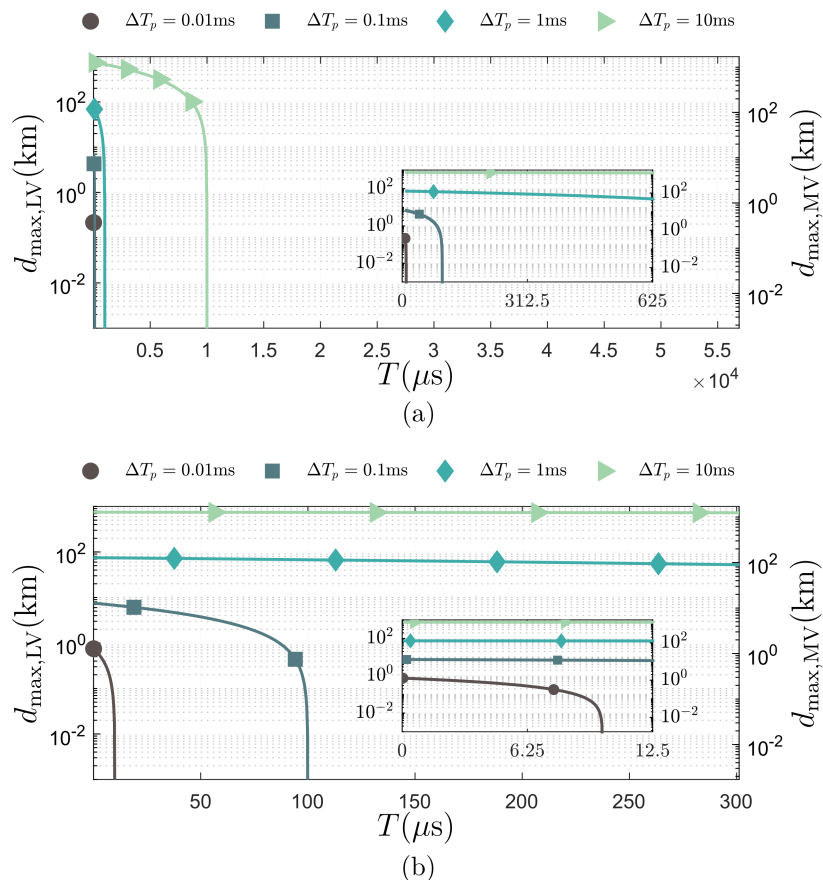

Figure 15: Maximum unambiguous range $d_{\max,\text{LV}}$ and $d_{\max,\text{MV}}$ for respectively LV and MV scenarios as a function of the pulse duration T for (a) NB-PLC and (b) BB-PLC systems.

6.1.1 Regulatory compliance

Although proper resolution and maximum unambiguous range can be achieved through an efficient project of the pulse to be injected into the distribution network, regulatory constraints reduce the degree of freedom of this project and therefore limits the set of possible T, Δd, and $d_{\max}$ values. In this sense, an analysis covering the NB regulations European Committee for Electrotechnical Standardization (*Comité Européen de Normalisation Électrotechnique* in French) (CENELEC), Association of Radio Industries and Businesses (ARIB), and Federal Communications Commission (FCC) is carried out, whereas European and Brazilian regulations [75, 76] and the HomePlug AV2 extended frequency band [77] are considered for the BB case. In this analysis, frequency bands from zero to the frequency upper bound of each regulation are considered, achieving $B = 1412.750$ kHz, $B = 450$ kHz, and $B = 490$ kHz for CENELEC, ARIB, and FCC, and $B = 30$ MHz, $B = 50$ MHz, and $B = 86$ MHz for the European and Brazilian regulations, and the HomePlug AV2 specification. Based on these considerations, Table 5 presents the pulse duration for each of the considered regulations. As expected from the analysis from Figure 13, pulses associated with shorter frequency bandwidths present longer duration.

The resulting range resolution Δd for the considered pulses in the considered LV and MV scenarios are presented in Table 6. The attained results reinforce the suitability of BB pulses only for very short sections of distribution networks. In spite of providing fine resolution, these pulses occupy rather long frequency bandwidths that tend to result in larger attenuation of the injected signal, which becomes unpractical in long LV distribution networks or MV distribution networks in general. NB pulses that comply with the considered regulations, in their turn, are appropriate for most scenarios, with the HS-OFDM and CSS pulses in the FCC band offering the finest resolution in both LV and MV scenarios. UWB pulses, however, must be used with care due to their great level of sidelobes.

Assuming a desired maximum unambiguous range $d_{\max} = 1$ km for LV distribution networks and $d_{\max} = 10$ km for LV distribution networks, Table 7 shows the necessary pulse repetition interval ΔT for the analyzed PLC pulses with durations presented in Table 5. As same duration T for the HS-OFDM and CSS pulses is considered, they require same pulse repetition interval. Such rate is considerably longer than the ones required for UWB pulses, with the difference between them decreasing as the frequency bandwidth B increases. This means that, although UWB pulses offer a worse performance in terms of PSLR, ISLR, and even range resolution Δd, their adoption allows the acquisition of a very larger number of reflectograms in a given time interval than if HS-OFDM or CSS pulses are adopted.

Table 5: Pulse duration T associated with regulations for NB- and BB-PLC systems.

Pulse duration T (μs)				
		CENELEC	**ARIB**	**FCC**
NB-PLC	**HS-OFDM**	3447.81	1137.78	1044.90
	UWB-1	24.00	7.92	7.27
	UWB-2	26.62	8.78	8.07
	CSS	3447.81	1137.78	1044.90
		European	**Brazilian**	**HomePlug**
BB-PLC	**HS-OFDM**	17.07	10.24	5.95
	UWB-1	0.12	0.07	0.04
	UWB-2	0.13	0.08	0.05
	CSS	17.07	10.24	5.95

Table 6: Range resolution Δd associated with regulations for NB- and BB-PLC systems.

Range resolution Δd (m)					
			CENELEC	**ARIB**	**FCC**
NB-PLC	**LV**	**HS-OFDM**	504.71	166.56	152.96
		UWB-1	726.81	239.85	220.27
		UWB-2	598.07	197.36	181.25
		CSS	504.71	166.56	152.96
	MV	**HS-OFDM**	863.60	284.99	261.72
		UWB-1	1243.63	410.40	376.90
		UWB-2	1023.34	337.70	310.13
		CSS	863.60	284.99	261.72
			European	**Brazilian**	**HomePlug**
BB-PLC	**LV**	**HS-OFDM**	2.50	1.50	0.87
		UWB-1	3.60	2.16	1.25
		UWB-2	2.96	1.78	1.03
		CSS	2.50	1.50	0.87
	MV	**HS-OFDM**	4.27	2.56	1.49
		UWB-1	6.16	3.69	2.15
		UWB-2	5.07	3.04	1.77
		CSS	4.27	2.56	1.49

Table 7: Pulse repetition interval ΔT associated with $d_{\max} = 1$ km for the LV scenario and $d_{\max} = 10$ km for the MV scenario complying with regulations for NB- and BB-PLC systems.

Pulse repetition interval ΔT (μs)					
			CENELEC	**ARIB**	**FCC**
NB-PLC	**LV**	**HS-OFDM**	3461.15	1151.12	1058.24
		UWB-1	37.34	21.26	20.62
		UWB-2	39.96	22.13	21.41
		CSS	3461.15	1151.12	1058.24
	MV	**HS-OFDM**	3525.79	1215.75	1122.87
		UWB-1	101.98	85.90	85.25
		UWB-2	104.59	86.76	86.04
		CSS	3525.79	1215.75	1122.87
			European	**Brazilian**	**HomePlug**
BB-PLC	**LV**	**HS-OFDM**	30.41	23.58	19.30
		UWB-1	13.46	13.41	13.38
		UWB-2	13.47	13.42	13.39
		CSS	30.41	23.58	19.30
	MV	**HS-OFDM**	95.04	88.22	83.93
		UWB-1	78.09	78.05	78.02
		UWB-2	78.11	78.05	78.02
		CSS	95.04	88.22	83.93

6.2 ANALYSIS OF MULTICARRIER TDR FOR POWER LINE SENSING BASED ON HS-OFDM AND OCDM SCHEMES

In this section, the carried out discussion on multicarrier TDR systems based on HS-OFDM and OCDM schemes in Chapters 4 and 5 is validated via numerical results. Given this context, Subsection 6.2.1 compares the pulse compression and channel estimation reflectogram processing approaches for HS-OFDM-based TDR systems, while Subsection 6.2.2 assesses limitations of both HS-OFDM- and OCDM-based TDR systems in terms of range resolution and maximum unambiguous range. Finally, the discussed HS-OFDM- and OCDM-based multiple access schemes are compared in Subsection 6.2.3.

6.2.1 Pulse compression and channel estimation comparison

In order to corroborate with the claim that channel estimation procedure outperforms the digital pulse compression for TDR, Figures 16a and 16b present a computational complexity comparison between both approaches in terms of $\times/\div$ operations and $+/-$ operations, respectively. Based on the information provided in Table 1, a far higher com-

putational complexity is demanded by the pulse compression approach as it is performed on a longer vector.
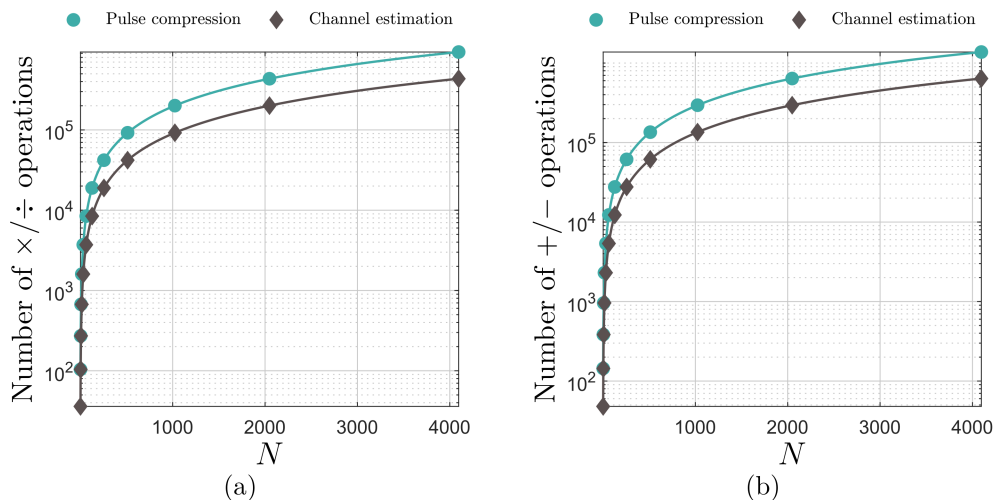
Figure 16: Computational complexity in terms of (a) $\times/\div$ operations and (b) $+/-$ operations as a function of N for the two reflectogram processing approaches.

Furthermore, the claim that the quality of obtained reflectograms is higher if channel estimation is adopted is endorsed by the results from Figures 17 and 18. In these figures, PSLR and ISLR values are respectively shown for the equivalent transmit pulse $s(t) = R_{xx}(t)$ obtained via pulse compression and the equivalent transmit pulse $s(t) = Bsinc(Bt)$ for channel estimation. In this figure, typical digital modulations schemes for PLC systems, namely BPSK, quadrature phase-shift keying (QPSK), and eight phase-shift keying (8PSK) [71], are considered for pulse compression, being the results for the channel estimation approach independent of the adopted scheme.
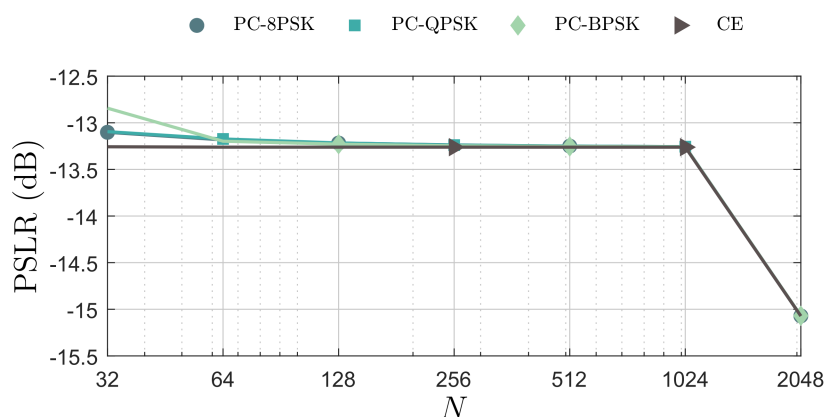
Figure 17: PSLR as a function of the number of subcarriers N for the digital pulse compression with BPSK, QPSK, and 8PSK digital modulations, and for channel estimation.

The attained results show that the PSLR decreases with the digital modulation order for the pulse compression approach. As N increases, the difference among the
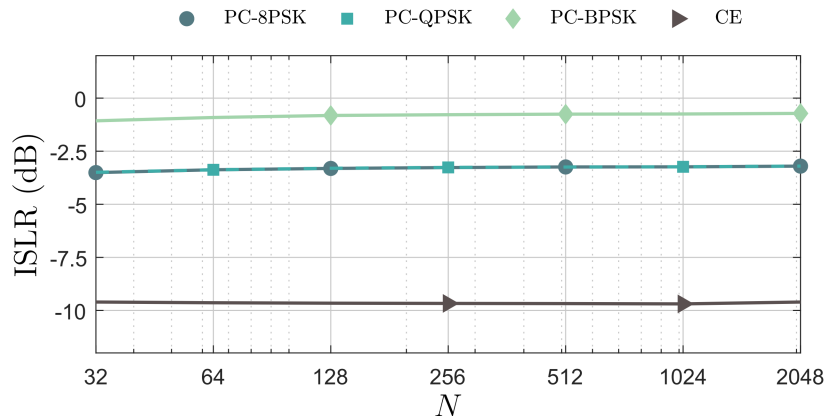
Figure 18: ISLR as a function of the number of subcarriers N for the digital pulse compression with BPSK, QPSK, and 8PSK digital modulations, and for channel estimation.

PSLR values yielded by either pulse compression or channel estimation becomes negligible. Finally, it is observed that PSLR levels decrease inversely along with N.

Regarding ISLR, the attained values also decrease with the digital modulation order for pulse compression, being the difference between QPSK and 8PSK more subtle. The best ISLR values are attained by channel estimation, which significantly outperforms the pulse compression approach by about 6.4 dB if QPSK and 8PSK are assumed for the latter, and by 8.9 dB if pulse compression is performed on a signal belonging to a BPSK modulation. Unlike the PSLR case, there is a slight increase of ISLR values along with N. This is explained by the fact that, given a fixed frequency bandwidth B, the integrated side lobe level is increased, while the main lobe duration of $1/(2B)$ seconds and therefore the main lobe level are maintained for longer HS-OFDM symbols.

6.2.2 Multicarrier TDR system limitations

Although an adequate parametrization of the HS-OFDM-based TDR system can yield valid reflectograms, regulatory constraints limit PSLR and ISLR, as well as range resolution and maximum unambiguous range values. The latter two parameters are also influenced by characteristics of the cable where the injected signal propagates, which define the phase velocity v_p. An awareness of such limitations is therefore paramount for performing adequate sensing of the power distribution network. In this context, the considered scenarios are the European underground LV and the US overhead MV power distribution networks described in Section 6.1, whose per unit length parameters and associated phase velocity are listed in Table 2.

Figure 19 shows the range resolution Δd as a function of the occupied frequency bandwidth B for the considered LV and MV scenarios. The achieved Δd values range from tens of thousands of kilometers for low B values to a few meters for higher B values, with a ratio of 1.71 between the resolution in the MV and LV and scenarios due to their

different phase velocity. The presented results indicate that B values in the NB-PLC frequency range, i.e., $B < 500$ kHz, result in fair range resolution values, i.e., $\Delta d \geq 75$ m, and therefore a fair capability of resolving close impedance discontinuities for typical distances covered by PLC signaling in LV and MV power distribution networks, which are about 1 km in MV scenarios and shorter in LV scenarios [23, 73].
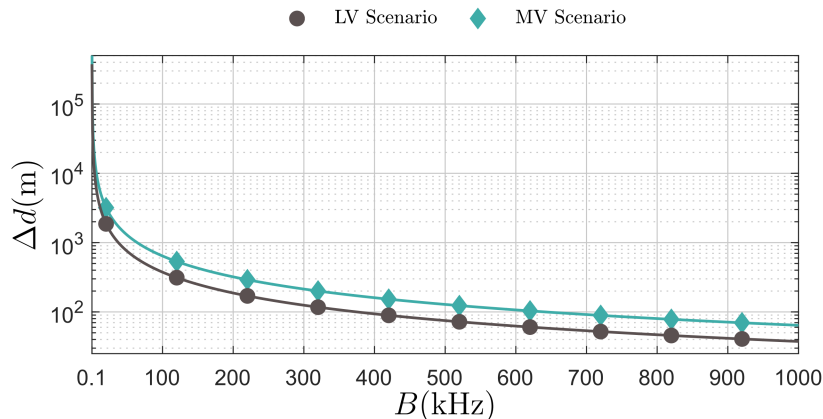
Figure 19: Range resolution Δd in meters as a function of the occupied frequency bandwidth B in the considered LV and MV scenarios.

For typical OFDM-based PLC systems [61, 78], one observes $2N > L_{cp}$. As a consequence, only L_{cp} limits $d_{\max}$ according to the relation in (4.7). Based on this assumption and considering typical sampling frequency values for NB-PLC, namely $F_s = 0.4$ MHz and $F_s = 1.2$ MHz [71], Figure 20 shows the maximum unambiguous range $d_{\max}$ as a function of the cyclic prefix length in the considered LV and MV scenarios. In this figure, one observes a minimum $d_{\max}$ value of about 1 km for $L_{cp} \geq 16$, which is experienced with $F_s = 1.2$ MHz in the LV scenario. For $L_{cp} \geq 64$, it holds $d_{\max} \geq 4$ km for both considered sampling frequencies in both LV and MV scenarios. As the typical spacing between PLMs in a power distribution network is considerably shorter than that, these results show that typical cyclic prefix lengths for NB-PLC systems, i.e., $L_{cp} = 32$ and $L_{cp} = 50$, are enough for providing fair maximum unambiguous range values.

Focusing on regulatory constraints, Appendix B assesses the performance of HS-OFDM-based TDR systems under FCC, ARIB, and CENELEC regulation constraints, which are addressed in the IEEE 1901.2 Standard [71] for NB-PLC. Such analysis is not performed for OCDM-based TDR systems since their spread spectrum characteristic prevents the insertion of frequency guard bands as recommended by the aforementioned regulations.

6.2.3 Comparison of multiple access schemes for enabling distributed power line sensing

In this subsection, a comparison among the three HS-OFDM-based multiple access schemes described in Section 4.4 and the OCDM-based multiple access scheme from
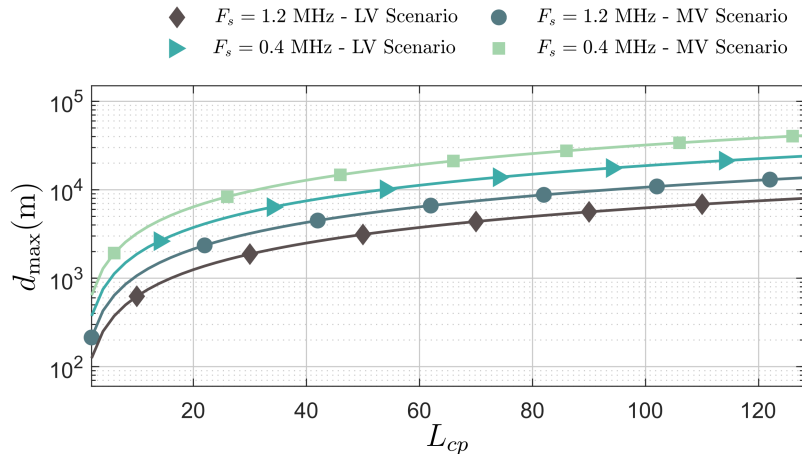
Figure 20: Maximum unambiguous range $d_{\max}$ as a function of cyclic prefix length L_{cp} for a sampling frequency $F_s = 1.2$ MHz.

Section 5.2 is carried out. For this purpose, the system parameters listed in Table 8 are adopted. Additionally, an multiconductor transmission line (MTL)-based model [5, 79] of a real MV power distribution network section in the city of Curitiba, Brazil, depicted in Figure 21 is considered. This section is consisted by a feeder, which is an high-voltage (HV)/MV transformer, followed by 2.73 km of line and a delta load. The input impedance of the HV/MV transformer at the MV side, as well as the input impedance of the network after the delta load are assumed to be much higher than the characteristic impedance of the line, thus behaving as an open circuit. Two PLMs are connected to this network right after the feeder, being one connected between phases A and B and the other between phases C and B. After an 1 km line section, other PLMs are connected to the network between the same pairs of phases. Thus, there is a line section with length of 1.73 km between the latter PLMs and the delta load. Finally, the adopted additive noise model is the one reported in [75, 80], whose one-sided PSD in the continuous-frequency domain is $S_V(f) = -93 + 52.98e^{-0.0032f/10^3}$ dBm/Hz.

Table 8: Adopted multicarrier TDR system parameters for comparison of multiple access schemes.

Multicarrier TDR system parameters		
Frequency range (kHz)		$0 - 500$
Frequency bandwidth B (kHz)		500
Sampling frequency F_s (MHz)		1
OCDM symbol length $2N$		256
Cyclic prefix length L_{cp}	Standard	30
	Long	52
Transmit signal PSD (dBm/Hz)		-40
Modulation scheme		BPSK
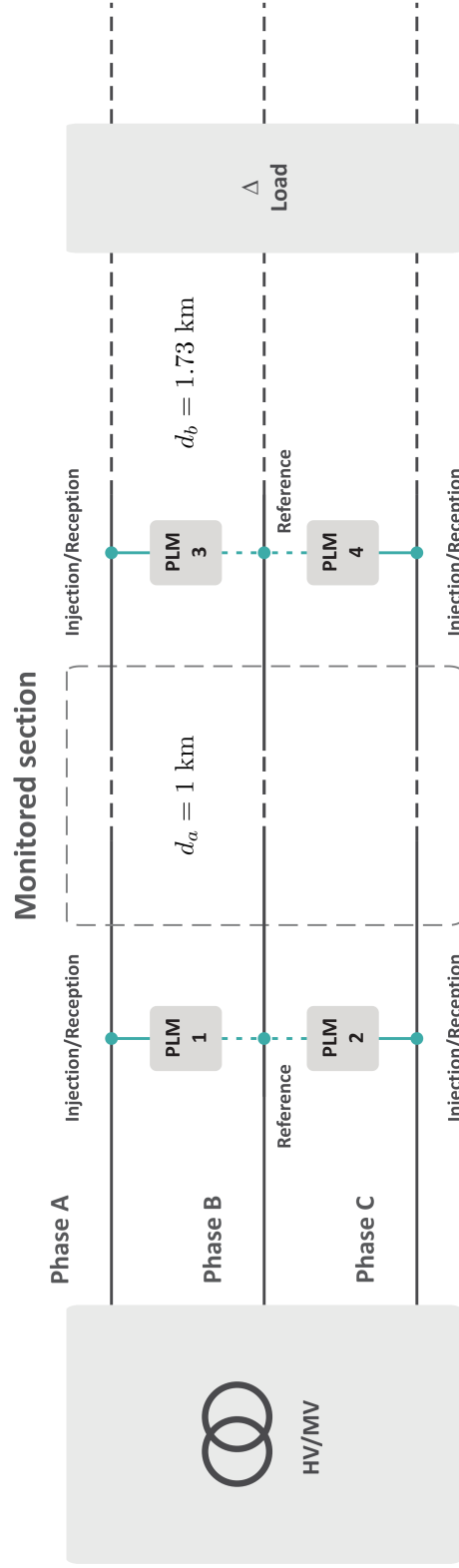
Figure 21: Representation of an MV distribution network section in the city of Curitiba, Brazil.

The number of reflectograms obtained over time $N_{\rho,i}$, $i \in \{TDMA, FDMA, CDMA, OCDM\}$, for the considered multiple access schemes as a function of N_{PLM} is shown in Figure 22a for $L_{cp} = 30$ and in Figure 22b for $L_{cp} = 52$. In these figures, one observes decreasing number of obtained reflectograms along with N_{PLM} for both HS-OFDM/TDMA and HS-OFDM/CDMA schemes, while HS-OFDM/FDMA and the proposed OCDM-based multiple access schemes obtain a constant number of reflectograms regardless of the number N_{PLM} of PLMs. This happens due to the long time interval during which a PLM does not transmit signals in the HS-OFDM/TDMA scheme. The lower N_{ρ} values in the HS-OFDM/CDMA scheme are on the other hand due to the spreading of HS-OFDM symbols, which results in longer effective transmission time for HS-OFDM symbols in this scheme.It is worth highlighting that, in the HS-OFDM/FDMA, the obtained reflectograms by each PLM will be distorted if the number N/N_{PLM} of subcarriers assigned to each of them ($128/N_{PLM}$ in the considered case) does not satisfy both the reflection channel coherence bandwidth constraint from (4.6) and the maximum unambiguous range constraint from (4.8), being the latter only relevant if $2N/N_{PLM} < L_{cp}$ due to the relationship from (4.7).
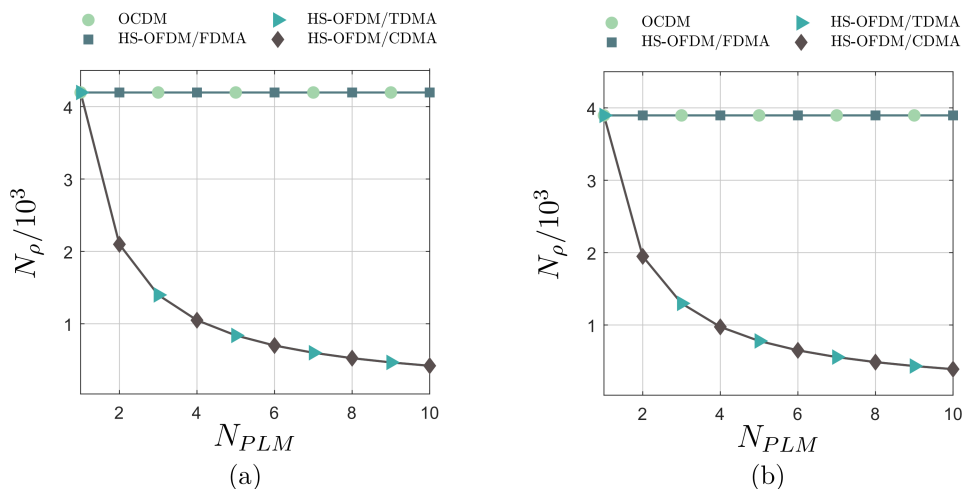
Figure 22: Number of obtained reflectograms N_{ρ} as a function of the number of PLMs N_{PLM} for (a) $L_{cp} = 30$, and (b) $L_{cp} = 52$.

The attained number of transferograms over time N_{τ} is shown Figure 23a for $L_{cp} = 30$ and in Figure 23b for $L_{cp} = 52$. As expected according to (5.11), no transferogram is obtained for $N_{PLM} = 1$. The presented results also show rapidly increasing N_{τ} values along with N_{PLM} for the proposed OCDM-based scheme and HS-OFDM/FDMA, while HS-OFDM/TDMA and HS-OFDM/CDMA yield slower increasing N_{τ} along with N_{PLM}. The reasons for such behavior are the same as in the case of reflectograms.

A further analysis is a comparison of the HS-OFDM-based TDMA, FDMA, and CDMA multiple access schemes and the proposed OCDM-based multiple access scheme adopting the SINR of the discrete-frequency domain received vector $\mathbf{Y}$ was adopted as
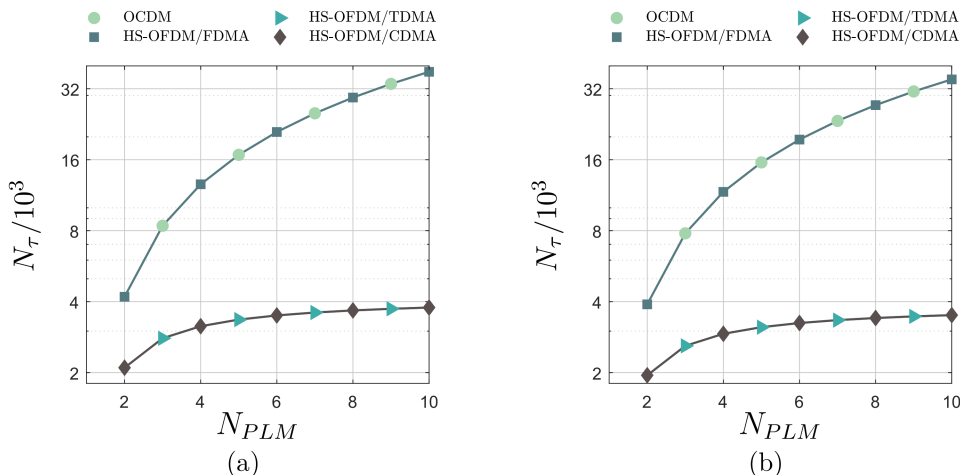
Figure 23: Number of obtained transferograms N_τ as a function of the number of PLMs N_{PLM} for (a) $L_{cp} = 30$, and (b) $L_{cp} = 52$.

a metric. The assumption of the system parameters listed in Table 8 results in total transmission power values of 20 dBm for the proposed OCDM-based multiple access scheme as well as the HS-OFDM/TDMA and HS-OFDM/CDMA schemes, while the total transmission power for the HS-OFDM/FDMA scheme is 13.98 dBm due its smaller number of active subcarriers at each PLM.

For the proposed OCDM-based multiple access scheme, as well as for HS-OFDM/TDMA and HS-OFDM/FDMA schemes, the SINR for each PLMs is equal to the ratio between the total received signal power and the total additive noise power, being equivalent the overall SNR considering the allocated subchirps/subcarriers to them. The CDMA case, on the other hand, has also an interference noise term resulting from the decoding process from (4.20) and pointed out in (4.21). As a consequence, the SINR at the four PLMs is equal to the ratio between their associated total received signal power and the total additive noise plus interference noise power.

The attained SINR values are listed in Table 9. The lower SINR experienced by the PLMs in the OCDM and HS-OFDM/TDMA schemes is due to the fact that the whole additive noise spectral content impairs the captured signal that they receive from the reflection channel. Meanwhile, the subcarrier hopping in the HS-OFDM/FDMA scheme results in higher SINR. This is due to the fact that greater part of the additive noise power is concentrated in lower frequencies as its PSD decreases exponentially. As a consequence, the subcarrier hopping makes the PLMs experience less effective noise power and therefore increases the SINR in comparison to the OCDM-based and HS-OFDM/TDMA multiple access schemes. The increasing SINR along with the PLM index u is due to the fact that subcarriers belonging to the set $\mathcal{K}_u$ allocated to the uth PLM are associated to higher frequency bins $f_k = k\Delta f$ as u increases, which is described in Subsection 4.4.2 and results in lower effective additive noise power for higher u. Finally, the higher average

SINR among the PLMs in the HS-OFDM/CDMA scheme is due to the SNR gain due to noise averaging in the decoding process, as described in Subsection 4.4.3.

Table 9: SINR of the reflectograms at the four PLMs for the considered multiple access schemes.

	SINR (dB)			
	PLM 1	**PLM 2**	**PLM 3**	**PLM 4**
OCDM	14.85	14.85	14.85	14.85
HS-OFDM/TDMA	14.85	14.85	14.85	14.85
HS-OFDM/FDMA	13.83	14.54	15.28	16.04
HS-OFDM/CDMA	17.87	17.87	17.87	17.87

7 CONCLUSIONS

This thesis has discussed key aspects of typical PLC pulses for fault sensing in power lines via pulse-compression TDR. In summary, the fault sensing system has been described, closed-form expressions for the compressed PLC pulses have been presented, and performance metrics usually adopted for radar systems have been used for assessing the suitability of the analyzed signals for TDR purposes. Comparative analysis considering two scenarios, namely an European underground LV distribution network and an US overhead MV distribution network, have been carried out for HS-OFDM, impulsive UWB, and CSS pulses of same time duration in terms of occupied frequency bandwidth, range resolution, and pulse repetition interval. This analysis is concluded with a discussion addressing NB and BB PLC regulatory compliance.

Based on the obtained results, one can see that the use of impulsive UWB pulses, i.e., the first and the second derivatives of the Gaussian pulse, enables the obtaining of a higher number of reflectograms due to their short time duration for pulse-compression TDR. However, the pulse compression for this class of signals is not nearly as effective as for HS-OFDM and CSS pulses, resulting therefore in poorer range resolution enhancement. It has also been revealed that the best PSLR value is achieved by CSS pulses, followed by HS-OFDM, first derivative of the Gaussian pulse, and second derivative of the Gaussian pulse, in this order. With respect to ISLR, the best performance is achieved by HS-OFDM pulses, followed by the second derivative of the Gaussian pulse, CSS pulses and the first derivative of the Gaussian pulse, in this order. Based on the PSLR values, one can conclude that the use of HS-OFDM and CSS pulses results in reflectograms with less distortion. The relevant ISLR value for HS-OFDM and CSS pulses in comparison with the second derivative of the Gaussian pulse is explained by the higher PCR achieved by the former, which makes the integrated sidelobe level higher although the sidelobes have, individually, lower level than in UWB pulses. Table 10 shows a summary of the achieved results for typical PLC pulses for pulse-compression TDR. Their performances are compared in a qualitative manner rather than quantitatively.

Table 10: Performance summary of typical PLC pulses for pulse-compression TDR.

Pulse	No. of reflectograms over time for fixed T	Δd for fixed B	PCR	Reflectogram distortion
HS-OFDM	●○○○○	●●●●●	●●●●●	●●●●◐
UWB-1	●●●●◐	◐○○○○	◐○○○○	●○○○○
UWB-2	●●●●●	●○○○○	●○○○○	◐○○○○
CSS	●○○○○	●●●●●	●●●●●	●●●●●

Furthermore, exploitation of multicarrier properties of the HS-OFDM scheme for

TDR purposes has been investigated. In this context, channel estimation has been introduced as an alternative to the usual pulse compression. Also, the use of TDMA, FDMA, and CDMA schemes for enabling distributed power line sensing has been investigated. The carried out discussion has been supported by a comparative analysis between channel estimation and pulse compresion. Also, the influence of the HS-OFDM-based TDR system parametrization on sidelobe level, range resolution, and maximum unambiguous range has been discussed for the aforementioned European LV and US MV scenarios, and the considered multiple access schemes have been compared considering a Brazilian overhead MV scenario.

Finally, an OCDM-based TDR system has been introduced for power line sensing along with a multiple access scheme relying on the convolution theorem of the modified DFnT from Type-III OCDM [34], which overcomes the need for complex synchronization from HS-OFDM/TDMA, the loss of spectral content from HS-OFDM/FDMA, and the obtaining of small number of measurements over time from HS-OFDM/CDMA. As in the HS-OFDM case, the influence of the TDR system parameters on its performance has been analyzed. The proposed OCDM-based multiple access is then compared with its HS-OFDM-based counterparts.

The attained results for multicarrier-based TDR systems show that the NB-PLC frequency range is suitable for sensing of LV and MV power distribution networks, with the appropriate frequency bandwidth for monitoring a power distribution network section being inversely proportional to its length. For this analysis, typical European underground LV and US overhead MV scenarios have been considered and compliance to FCC, ARIB, and CENELEC NB-PLC regulations has also been addressed. Finally, it has been shown that the proposed OCDM-based multiple access scheme performs equally to the HS-OFDM/TDMA scheme in terms of SINR. In comparison to the HS-OFDM/FDMA scheme, the OCDM-based scheme performs better for 2 PLM and worse for the other 2 PLM due to the combined effect of subcarrier hopping and exponentially decaying PSD that increases or decreases the SINR for different PLMs in the former scheme. The best SINR performance, however, is still attained by the HS-OFDM/CDMA scheme due to its averaging process that reduces the effective additive noise power. Table 11 shows a summary of the achieved results for multicarrier-based multiple access schemes for distributed power line sensing via TDR, comparing their performances in a qualitative manner.

Table 11: Performance summary of multicarrier-based multiple access schemes for distributed power line sensing via TDR.

Pulse	No. of measurements over time for fixed T	Average SINR performance
HS-OFDM/TDMA	●●○○○	●●●●○
HS-OFDM/FDMA	●●●●●	●●●○○
HS-OFDM/CDMA	●●○○○	●●●●●
OCDM	●●●●●	●●●●○

REFERENCES

[1] F. Passerini and A. M. Tonello, "Smart grid monitoring using power line modems: Effect of anomalies on signal propagation," *IEEE Access (Early Access)*, pp. 1–9, June 2019.

[2] M. Sedighizadeh, A. Rezazadeh, and N. I. Elkalashy, "Approaches in high impedance fault detection - a chronological review," *Advances in Electrical and Computer Engineering*, vol. 10, no. 3, pp. 114–128, Aug 2010.

[3] A. Ghaderi, H. L. Ginn, and H. A. Mohammadpour, "High impedance fault detection: A review," *Electric Power Systems Research*, vol. 143, pp. 376 – 388, Feb. 2017.

[4] F. Auzanneau, "Wire troubleshooting and diagnosis: Review and perspectives," *Progress In Electromagnetics Research B*, vol. 49, pp. 253–279, 2013.

[5] C. R. Paul, *Analysis of Multiconductor Transmission Lines, 2nd Edition.* John Wiley & Sons Inc., 2007.

[6] C. Furse, Y. Chung, C. Lo, and P. Pendayala, "A critical comparison of reflectometry methods for location of wiring faults," *Smart Structures and Systems*, vol. 2, no. 1, pp. 25–46, Jan. 2006.

[7] J. Wang, P. E. C. Stone, Y.-J. Shin, and R. A. Dougal, "Application of joint time-frequency domain reflectometry for electric power cable diagnostics," *IET Signal Processing*, vol. 4, no. 4, pp. 395–405, Aug. 2010.

[8] L. G. da S. Costa, A. C. M. de Queiroz, B. Adebisi, V. L. R. da Costa, and M. V. Ribeiro, "Coupling for power line communication: A survey," *Journal of Communication and Information Systems*, vol. 32, no. 1, March 2017.

[9] M. de L. Filomeno, G. R. Colen, L. G. de Oliveira, and M. V. Ribeiro, "Two-stage single-relay channel model for in-home broadband PLC systems," *IEEE Systems Journal*, vol. 13, no. 1, pp. 204–214, March 2019.

[10] G. R. Colen, C. A. G. Marques, T. R. Oliveira, F. P. V. de Campos, and M. Ribeiro, "Measurement setup for characterizing low-voltage and outdoor electric distribution grids for PLC systems," in *Proc. IEEE PES Conference On Innovative Smart Grid Technologies Latin America*, Apr. 2013, pp. 1–5.

[11] G. R. Colen, H. Schettino, D. Fernandes, L. M. Sirimarco, F. P. V. de Campos, W. A. Finamore, H. A. Latchman, and M. V. Ribeiro, "A temporal compressive resource allocation technique for complexity reduction in PLC transceivers," *Trans. on Emerging Telecommunications Technologies*, 2015.

[12] G. R. Colen, L. G. de Oliveira, A. A. M. Picorone, T. R. Oliveira, C. B. Zeller, A. J. Han Vinck, and M. V. Ribeiro, "A new parameter for computational complexity reduction in resource allocation for PLC systems," *Manuscript in progress*, vol. n/a, no. n/a, pp. n/a–n/a, n/a 2015.

[13] G. R. Colen, L. G. de Oliveira, A. J. H. Vinck, and M. V. Ribeiro, "Resource allocation in OFDM-based PLC systems impaired by additive impulsive gaussian noise,"

in *2016 IEEE International Symposium on Power Line Communications and its Applications (ISPLC)*, Mar. 2016, pp. 70–75.

[14] L. G. de Oliveira, G. R. Colen, M. V. Ribeiro, and A. J. H. Vinck, "Narrow-band interference error correction in coded ofdm-based plc systems," in *2016 International Symposium on Power Line Communications and its Applications (ISPLC)*, March 2016, pp. 13–18.

[15] G. R. Colen, L. G. de Oliveira, C. B. Zeller, A. J. Han Vinck, and M. V. Ribeiro, "Statistical analysis and modeling of a novel parameter for resource allocation in multicarrier PLC systems," *Transactions on Emerging Telecommunications Technologies*, vol. 28, no. 11, pp. e3180–n/a, November 2017.

[16] M. S. P. Facina, H. A. Latchman, H. V. Poor, and M. V. Ribeiro, "Cooperative in-home power line communication: Analyses based on a measurement campaign," *IEEE Transactions on Communications*, vol. 64, no. 2, pp. 778–789, Feb 2016.

[17] S. Galli, A. Scaglione, and Z. Wang, "For the grid and through the grid: The role of power line communications in the smart grid," *Proceedings of the IEEE*, vol. 99, no. 6, pp. 998–1027, June 2011.

[18] L. de M. B. A. Dib, V. Fernandes, M. de L. Filomeno, and M. V. Ribeiro, "Hybrid PLC/wireless communication for smart grids and internet of things applications," *IEEE Internet of Things Journal*, vol. 5, no. 2, pp. 655–667, April 2018.

[19] R. M. Oliveira, A. B. Vieira, H. A. Latchman, and M. V. Ribeiro, "Medium access control protocols for power line communication: A survey," *IEEE Communications Surveys Tutorials (Early Access)*, pp. 1–19, August 2018.

[20] M. Wollschlaeger, T. Sauter, and J. Jasperneite, "The future of industrial communication: Automation networks in the era of the internet of things and industry 4.0," *IEEE Industrial Electronics Magazine*, vol. 11, no. 1, pp. 17–27, March 2017.

[21] V. Fernandes, H. V. Poor, and M. V. Ribeiro, "A hybrid power line/wireless dual-hop system with energy harvesting relay," *IEEE Internet of Things Journal (Early Access)*, pp. 1–11, July 2018.

[22] A. Cataldo, E. de Benedetto, and G. Cannazza, *Broadband Reflectometry for Enhanced Diagnostics and Monitoring Applications.* Springer Berlin Heidelberg, 2011.

[23] F. Passerini and A. M. Tonello, "Smart grid monitoring using power line modems: Anomaly detection and localization," *IEEE Transactions on Smart Grid (Early Access)*, pp. 1–11, 2019.

[24] Y. Huo, G. Prasad, L. Lampe, and V. C. M. Leung, "Cable diagnostics with power line modems for smart grid monitoring," *Cornell University Library*, pp. 1–8, Aug. 2018. [Online]. Available: https://arxiv.org/abs/1808.01149

[25] F. Passerini and A. M. Tonello, "Power line fault detection and localization using high frequency impedance measurement," in *Proc. IEEE International Symposium on Power Line Communications and its Applications (ISPLC)*, April 2017, pp. 1–5.

[26] A. N. Milioudis, G. T. Andreou, and D. P. Labridis, "Detection and location of high impedance faults in multiconductor overhead distribution lines using power line communication devices," *IEEE Transactions on Smart Grid*, vol. 6, no. 2, pp. 894–902, March 2015.

[27] V. Taylor and M. Faulkner, "Line monitoring and fault location using spread spectrum on power line carrier," *IEE Proceedings - Generation, Transmission and Distribution*, vol. 143, no. 5, pp. 427–434, Sept. 1996.

[28] Z. Q. Bo, G. Weller, and M. A. Redfern, "Accurate fault location technique for distribution system using fault-generated high-frequency transient voltage signals," *IEE Proceedings - Generation, Transmission and Distribution*, vol. 146, no. 1, pp. 73–79, Jan 1999.

[29] F. de Paulis, C. Olivieri, A. Orlandi, and G. Giannuzzi, "Detectability of degraded joint discontinuities in HV power lines through TDR-like remote monitoring," *IEEE Transactions on Instrumentation and Measurement*, vol. 65, no. 12, pp. 2725–2733, Dec 2016.

[30] W. B. Hassen, F. Auzanneau, L. Incarbone, F. Pérès, and A. P. Tchangani, "Distributed sensor fusion for wire fault location using sensor clustering strategy," *International Journal of Distributed Sensor Networks*, vol. 11, no. 4, pp. 1–17, April 2015.

[31] L. G. de Oliveira, G. R. Colen, A. J. H. Vinck, and M. V. Ribeiro, "Resource allocation in HS-OFDM-based PLC systems: A tutorial," *Journal of Communication and Information Systems*, vol. 33, no. 1, Oct. 2018.

[32] M. L. G. Salmento, E. P. de Aguiar, A. Camponogara, and M. V. Ribeiro, "An enhanced receiver for an impulsive UWB-based PLC system for low-bit rate applications," *Digital Signal Processing*, vol. 70, pp. 145 – 154, 2017.

[33] A. M. Tonello, S. D'Alessandro, F. Versolatto, and C. Tornelli, "Comparison of narrow-band OFDM PLC solutions and I-UWB modulation over distribution grids," in *Proc. IEEE International Conference on Smart Grid Communications*, Oct. 2011, pp. 149–154.

[34] L. de M. B. A. Dib, "Multichirp code division multiple access for smart grids and internet of things," Master's thesis, Federal University of Juiz de Fora, Brazil, 2018.

[35] F. Passerini and A. M. Tonello, "In band full duplex PLC: The role of the hybrid coupler," in *Proc. International Symposium on Power Line Communications and its Applications*, Mar. 2016, pp. 52–57.

[36] F. Passerini and A. M. Tonello, "Full duplex power line communication modems for network sensing," in *Proc. IEEE International Conference on Smart Grid Communications*, Oct. 2017, pp. 213–217.

[37] F. Passerini and A. M. Tonello, "Adaptive hybrid circuit for enhanced echo cancellation in full duplex PLC," in *Proc. IEEE International Symposium on Power Line Communications and its Applications*, Apr. 2018, pp. 1–5.

[38] M. O. Ahmed and L. Lampe, "Power line network topology inference using frequency domain reflectometry," in *Proc. IEEE International Conference on Communications*, June 2012, pp. 3419–3423.

[39] M. O. Ahmed and L. Lampe, "Power line communications for low-voltage power grid tomography," *IEEE Transactions on Communications*, vol. 61, no. 12, pp. 5163–5175, Dec. 2013.

[40] A. N. Milioudis, G. T. Andreou, and D. P. Labridis, "Enhanced protection scheme for smart grids using power line communications techniques - part II: Location of high impedance fault position," *IEEE Transactions on Smart Grid*, vol. 3, no. 4, pp. 1631–1640, Dec. 2012.

[41] M. Kafal, A. Cozza, and L. Pichon, "Locating faults with high resolution using single-frequency TR-MUSIC processing," *IEEE Transactions on Instrumentation and Measurement*, vol. 65, no. 10, pp. 2342–2348, Oct. 2016.

[42] S. J. Chang, C. K. Lee, C. Lee, Y. J. Han, M. K. Jung, J. B. Park, and Y. Shin, "Condition monitoring of instrumentation cable splices using kalman filtering," *IEEE Transactions on Instrumentation and Measurement*, vol. 64, no. 12, pp. 3490–3499, Dec. 2015.

[43] M. A. Richards, J. A. Scheer, and W. A. Holm, *Principles of Modern Radar - Basic Principles*. Scitech Publishing Inc., 2010, vol. 1.

[44] C. L. Temes, "Sidelobe suppression in a range-channel pulse-compression radar," *IRE Transactions on Military Electronics*, vol. MIL-6, no. 2, pp. 162–169, April 1962.

[45] M.-G. D. Benedetto, *UWB Communication Systems: A Comprehensive Overview*. Hindawi Publishing Corporation, 2006.

[46] I. S. Gradshteyn and I. M. Ryzhik, *Table of Integrals, Series, and Products*. Academic Press, 1980.

[47] G. Lellouch, A. K. Mishra, and M. Inggs, "Design of OFDM radar pulses using genetic algorithm based techniques," *IEEE Transactions on Aerospace and Electronic Systems*, vol. 52, no. 4, pp. 1953–1966, Aug. 2016.

[48] J. L. Eaves and E. K. Reedy, *Principles of Modern Radar*. Springer-Verlag US, 1987.

[49] S. Naik, C. M. Furse, and B. Farhang-Boroujeny, "Multicarrier reflectometry," *IEEE Sensors Journal*, vol. 6, no. 3, pp. 812–818, June 2006.

[50] P. Amini, C. Furse, and B. Farhang-Boroujeny, "Filterbank multicarrier reflectometry for cognitive live wire testing," *IEEE Sensors Journal*, vol. 9, no. 12, pp. 1831–1837, Dec. 2009.

[51] A. Lelong and M. O. Carrion, "On line wire diagnosis using multicarrier time domain reflectometry for fault location," in *Proc. IEEE SENSORS*, Oct. 2009, pp. 751–754.

[52] T. R. Oliveira, C. A. G. Marques, W. A. Finamore, S. L. Netto, and M. V. Ribeiro, "A methodology for estimating frequency responses of electric power grids," *Journal of Control, Automation and Electrical Systems*, vol. 25, no. 6, pp. 720–731, Dec. 2014.

[53] A. Lelong, L. Sommervogel, N. Ravot, and M. O. Carrion, "Distributed reflectometry method for wire fault location using selective average," *IEEE Sensors Journal*, vol. 10, no. 2, pp. 300–310, Feb. 2010.

[54] S. K. Mitra, *Digital Signal Processing: A Computer-Based Approach, 4th Edition*. McGraw-Hill, 2010.

[55] W. B. Hassen, M. Kafal, and E. Cabanillas, "Time reversal applied to multi-carrier reflectometry for on-line diagnosis in complex wiring systems," in *Proc. IEEE AUTOTESTCON*, Sept. 2018, pp. 1–7.

[56] C. Sturm, E. Pancera, T. Zwick, and W. Wiesbeck, "A novel approach to OFDM radar processing," in *Proc. IEEE Radar Conference*, May 2009, pp. 1–4.

[57] L. G. de Oliveira, M. de L. Filomeno, L. F. Colla, H. V. Poor, and M. V. Ribeiro, "On the suitability of PLC pulses for power line fault sensing via time-domain reflectometry," *Cornell University Library*, pp. 1–13, Jan. 2019. [Online]. Available: https://arxiv.org/abs/1901.07923

[58] J. P. Fitch, *Synthetic Aperture Radar*, C. Burrus, Ed. Springer-Verlag, 1988.

[59] M. V. Ribeiro, G. R. Colen, F. V. de Campos, Z. Quan, and H. V. Poor, "Clustered-orthogonal frequency division multiplexing for power line communication: when is it beneficial?" *IET Communications*, vol. 8, pp. 2336–2347, Sept. 2014.

[60] Y. L. Sit, "MIMO OFDM radar-communication system with mutual interference cancellation," Ph.D. dissertation, Karlsruhe Institute of Technology, Germany, 2017.

[61] G. R. Colen, L. G. de Oliveira, A. J. H. Vinck, and M. V. Ribeiro, "A spectral compressive resource allocation technique for PLC systems," *IEEE Transactions on Communications*, vol. 65, no. 2, pp. 816–826, Feb. 2017.

[62] B. Nuss, J. Mayer, and T. Zwick, "Limitations of MIMO and multi-user access for OFDM radar in automotive applications," in *Proc. IEEE MTT-S International Conference on Microwaves for Intelligent Mobility*, April 2018, pp. 1–4.

[63] W. B. Hassen, "Étude de stratégies de diagnostic embarqué des réseaux filaires complexes," Ph.D. dissertation, University of Toulouse, France, 2014, in French.

[64] F. Auzanneau, "Transferometry: A new tool for complex wired networks diagnosis," *Progress In Electromagnetics Research B*, vol. 70, pp. 87–100, 2016.

[65] C. Sturm, Y. L. Sit, M. Braun, and T. Zwick, "Spectrally interleaved multi-carrier signals for radar network applications and multi-input multi-output radar," *IET Radar, Sonar Navigation*, vol. 7, no. 3, pp. 261–269, March 2013.

[66] X. Ouyang and J. Zhao, "Orthogonal chirp division multiplexing," *IEEE Transactions on Communications*, vol. 64, no. 9, pp. 3946–3957, Sep. 2016.

[67] X. Ouyang, O. A. Dobre, and J. Zhao, "Unbiased channel estimation based on the discrete fresnel transform for CO-OFDM systems," *IEEE Photonics Technology Letters*, vol. 29, no. 8, pp. 691–694, April 2017.

[68] X. Ouyang, C. Antony, G. Talli, and P. D. Townsend, "Robust channel estimation for coherent optical orthogonal chirp-division multiplexing with pulse compression and noise rejection," *Journal of Lightwave Technology*, vol. 36, no. 23, pp. 5600–5610, Dec. 2018.

[69] L. G. de Oliveira, M. de L. Filomeno, and M. V. Ribeiro, "HS-OFDM-based time-domain reflectometry for power line sensing: Characteristics and limitations," *Cornell University Library*, pp. 1–12, Jan. 2019. [Online]. Available: https://arxiv.org/abs/1901.08404

[70] L. Lampe and A. J. H. Vinck, "On cooperative coding for narrow band PLC networks," *AEU - International Journal of Electronics and Communications*, vol. 65, no. 8, pp. 681–687, Aug. 2011.

[71] "IEEE standard for low-frequency (less than 500 kHz) narrowband power line communications for smart grid applications," *IEEE Std 1901.2-2013*, pp. 1–269, Dec. 2013.

[72] S. Benson, C.-I. H. Chen, D. M. Lin, and L. L. Liou, "Digital linear chirp receiver for high chirp rates with high resolution time-of-arrival and time-of-departure estimation," *IEEE Transactions on Aerospace and Electronic Systems*, vol. 52, no. 3, pp. 1146–1154, June 2016.

[73] L. Lampe, A. M. Tonello, and T. G. Swart, *Power Line Communications: Principles, Standards and Applications from Multimedia to Smart Grid, 2nd Edition*. John Wiley & Sons Inc., 2016.

[74] R. Mohseni, A. Sheikhi, and M. A. Masnadi-Shirazi, "Multicarrier constant envelope OFDM signal design for radar applications," *International Journal of Electronics and Communications*, vol. 64, no. 11, pp. 999–1008, Nov. 2010.

[75] M. Girotto and A. M. Tonello, "EMC regulations and spectral constraints for multicarrier modulation in PLC," *IEEE Access*, vol. 5, pp. 4954–4966, Mar. 2017.

[76] ANATEL. (2009) Brazilian resolution for PLC. [Online]. Available: http://legislacao.anatel.gov.br/resolucoes/2009/101-resolucao-527

[77] L. Yonge, J. Abad, K. Afkhamie, L. Guerrieri, S. Katar, H. Lioe, P. Pagani, R. Riva, D. M. Schneider, and A. Schwager, "An overview of the HomePlug AV2 technology," *Journal of Electrical and Computer Engineering*, pp. 1–20, 2013.

[78] G. R. Colen, L. G. de Oliveira, C. B. Zeller, A. J. H. Vinck, and M. V. Ribeiro, "Statistical analysis and modeling of a novel parameter for resource allocation in multicarrier PLC systems," *Transactions on Emerging Telecommunications Technologies*, vol. 28, no. 11, pp. 1–12, May 2017.

[79] L. Franek and P. Fiedler, "A multiconductor model of power line communication in medium-voltage lines," *Energies*, vol. 10, no. 6, pp. 1–16, 2017.

[80] Z. Tao, Y. Xiaoxian, Z. Baohui, N. H. Xu, F. Xiaoqun, and L. Changxin, "Statistical analysis and modeling of noise on 10-kv medium-voltage power lines," *IEEE Transactions on Power Delivery*, vol. 22, no. 3, pp. 1433–1439, July 2007.

APPENDIX A – Proof of the Convolution Theorem of the Modified DFnT

The introduction of the modified DFnT starts with the diagonal matrix $\mathbf{\Gamma}_{2N} \in \mathbb{C}^{2N \times 2N}$. The elements $\Gamma_{k,k}$, $k = 0, \cdots, 2N - 1$ of $\mathbf{\Gamma}_{2N}$ are defined as

$$\Gamma_{k,k} \triangleq \begin{cases} e^{(-j\pi/2N)(k^2)}, & k \le N \\ e^{(j\pi/2N)(k^2)}, & k > N \end{cases}. \tag{A.1}$$

It clearly holds that $\mathbf{\Gamma}_{2N}\mathbf{\Gamma}_{2N}^{\dagger} = \mathbf{I}_{2N}$. The diagonal matrix $\mathbf{\Gamma}_{2N}$ inputs are the eigenvalues of a circulant matrix $\mathbf{\Phi}_{2N} \in \mathbb{R}^{2N \times 2N}$ such that

$$\mathbf{F}_{2N}\mathbf{\Phi}_{2N}\mathbf{F}_{2N}^{\dagger} = \mathbf{\Gamma}_{2N}, \tag{A.2}$$

where $\mathbf{F}_{2N} = (1/\sqrt{2N})\mathbf{W}_{2N}$. The real circulant matrix $\mathbf{\Phi}_{2N}$ from (A.2) is the modified DFnT matrix used for transforming $\mathbf{c} \in \mathbb{R}^{2N \times 2N}$ into the vector $\dot{\mathbf{c}} \in \mathbb{R}^{2N \times 2N}$ via the operation

$$\dot{\mathbf{c}} = \mathbf{\Phi}_{2N}\mathbf{c}, \tag{A.3}$$

The inverse DFnT is achieved therefore by

$$\mathbf{c} = \mathbf{\Phi}_{2N}^{\dagger}\dot{\mathbf{c}}. \tag{A.4}$$

The convolution theorem, as well as the unitary and the similarity transformation properties of the modified DFnT, on which the former is based, are demonstrated as follows.

Unitary property of the modified DFnT

For the circulant modified DFnT matrix $\mathbf{\Phi}_{2N}$ from (A.2), it holds the unitary property, i.e.,

$$\begin{aligned} \mathbf{\Phi}_{2N}^{\dagger}\mathbf{\Phi}_{2N} &= (\mathbf{F}_{2N}^{\dagger}\mathbf{\Gamma}_{2N}\mathbf{F}_{2N})(\mathbf{F}_{2N}^{\dagger}\mathbf{\Gamma}_{2N}^{\dagger}\mathbf{F}_{2N}) \\ &= \mathbf{I}_{2N}. \end{aligned} \tag{A.5}$$

Due to the Hermitian symmetry of $\mathbf{\Gamma}_{2N}$ observed in (A.1), one has that $\mathbf{\Phi}_{2N} \in \mathbb{R}^{2N \times 2N}$, which enables baseband applications for the presented DFnT matrix.

Similarity transformation of the modified DFnT

For the given circulant DFnT matrix, it also holds the similarity transformation expressed as

$$\mathbf{\Phi}_{2N}\mathbf{Z}\mathbf{\Phi}_{2N}^{\dagger} = \mathbf{Z}, \tag{A.6}$$

in which $\mathbf{Z} \in \mathbb{R}^{2N \times 2N}$ is a circulant matrix. The proof for (A.7) starts by rearranging the expression as

$$\boldsymbol{\Phi}_{2N} \mathbf{Z} \boldsymbol{\Phi}_{2N}^{\dagger} = (\mathbf{F}_{2N}^{\dagger} \boldsymbol{\Gamma}_{2N}^{\dagger} \mathbf{F}_{2N}) \mathbf{Z} (\mathbf{F}_{2N}^{\dagger} \boldsymbol{\Gamma}_{2N} \mathbf{F}_{2N}). \tag{A.7}$$

One can next write

$$\boldsymbol{\Phi}_{2N} \mathbf{Z} \boldsymbol{\Phi}_{2N}^{\dagger} = \mathbf{F}_{2N}^{\dagger} \boldsymbol{\Gamma}_{2N}^{\dagger} \boldsymbol{\Gamma}_{Z} \boldsymbol{\Gamma}_{2N} \mathbf{F}_{2N}, \tag{A.8}$$

in which $\boldsymbol{\Gamma}_{Z} = \mathbf{F}_{2N} \mathbf{Z} \mathbf{F}_{2N}^{\dagger}$ is a diagonal matrix whose inputs are the eigenvalues of the circulant matrix $\mathbf{Z}$. The pre- and post-multiplication of $\boldsymbol{\Gamma}_{Z}$ respectively by the diagonal matrices $\boldsymbol{\Gamma}_{2N}^{\dagger}$ and $\boldsymbol{\Gamma}_{2N}$ yields $\boldsymbol{\Gamma}_{2N}^{\dagger} \boldsymbol{\Gamma}_{Z} \boldsymbol{\Gamma}_{2N}$, which, as the three matrices are diagonal, becomes $\boldsymbol{\Gamma}_{2N}^{\dagger} \boldsymbol{\Gamma}_{2N} \boldsymbol{\Gamma}_{Z} = \boldsymbol{\Gamma}_{Z}$. (A.8) can then be rewritten as

$$\begin{aligned} \boldsymbol{\Phi}_{2N} \mathbf{Z} \boldsymbol{\Phi}_{2N}^{\dagger} &= \mathbf{F}_{2N}^{\dagger} \boldsymbol{\Gamma}_{Z} \mathbf{F}_{2N} \\ &= \mathbf{F}_{2N}^{\dagger} (\mathbf{F}_{2N} \mathbf{Z} \mathbf{F}_{2N}^{\dagger}) \mathbf{F}_{2N} \\ &= \mathbf{Z}, \end{aligned} \tag{A.9}$$

which proves (A.6).

Convolution theorem of the modified DFnT

Considering two vectors $\mathbf{a} \in \mathbb{R}^{2N \times 1}$ and $\mathbf{b} \in \mathbb{R}^{2N \times 1}$, to which are associated the circulant matrices $\mathbf{A} \in \mathbb{R}^{2N \times 2N}$ and $\mathbf{B} \in \mathbb{R}^{2N \times 2N}$, respectively, one can write the circular convolution between $\mathbf{a}$ and $\mathbf{b}$ as

$$\begin{aligned} \mathbf{c} &= \mathbf{A}\mathbf{b} \tag{A.10} \\ &= \mathbf{B}\mathbf{a}, \tag{A.11} \end{aligned}$$

where $\mathbf{c} \in \mathbb{R}^{2N \times 1}$. By applying the DFnT on $\mathbf{c}$, one obtains the vector $\dot{\mathbf{c}} \in \mathbb{R}^{2N \times 1} = \boldsymbol{\Phi}_{2N}\mathbf{c}$, which can be rewritten as

$$\begin{aligned} \dot{\mathbf{c}} &= \boldsymbol{\Phi}_{2N}\mathbf{A}\mathbf{b} \tag{A.12} \\ &= \boldsymbol{\Phi}_{2N}\mathbf{B}\mathbf{a}. \tag{A.13} \end{aligned}$$

Making use of the unitary and similarity transformation properties of the DFnT from (A.5) and (A.6), respectively, (A.12) and (A.13) can be further rearranged respectively as

$$\begin{aligned} \dot{\mathbf{c}} &= \boldsymbol{\Phi}_{2N}\mathbf{A}\boldsymbol{\Phi}_{2N}^{\dagger}\boldsymbol{\Phi}_{2N}\mathbf{b} \tag{A.14} \\ &= \boldsymbol{\Phi}_{2N}\mathbf{B}\boldsymbol{\Phi}_{2N}^{\dagger}\boldsymbol{\Phi}_{2N}\mathbf{a}. \tag{A.15} \end{aligned}$$

Using the similarity transformation property from (A.6), it is known that $\boldsymbol{\Phi}_{2N}\mathbf{A}\boldsymbol{\Phi}_{2N}^{\dagger} = \mathbf{A}$ and $\boldsymbol{\Phi}_{2N}\mathbf{B}\boldsymbol{\Phi}_{2N}^{\dagger} = \mathbf{B}$. Hence, (A.14) and (A.15) become, respectively,

$$\begin{aligned} \dot{\mathbf{c}} &= \mathbf{A}\boldsymbol{\Phi}_{2N}\mathbf{b} \tag{A.16} \\ &= \mathbf{B}\boldsymbol{\Phi}_{2N}\mathbf{a}. \tag{A.17} \end{aligned}$$

The terms $\boldsymbol{\Phi}_{2N}\mathbf{a}$ in (A.16) and $\boldsymbol{\Phi}_{2N}\mathbf{b}$ in (A.17) can be alternatively denoted by the vectors $\dot{\mathbf{a}} = \boldsymbol{\Phi}_{2N}\mathbf{a}$ and $\dot{\mathbf{b}} = \boldsymbol{\Phi}_{2N}\mathbf{b}$, respectively.

From (A.16) and (A.17), it is seen that the DFnT of the circular convolution between $\mathbf{a}$ and $\mathbf{b}$ can be interpreted as the circular convolution between $\mathbf{a}$ and $\dot{\mathbf{b}}$ or, alternatively, as the circular convolution between $\mathbf{b}$ and $\dot{\mathbf{a}}$.

APPENDIX B – Performance of regulatory-compliant, HS-OFDM-based TDR systems

The considered regulations for assessing the performance of HS-OFDM-based TDR systems are FCC, ARIB, and CENELEC, which are addressed in the IEEE 1901.2 Standard [71] for NB-PLC. The frequency range, occupied frequency bandwidth B, sampling frequency F_s, FFT/IFFT size, range and number of active subcarriers N_{active}, and cyclic prefix length L_{cp} associated with these regulations are listed in Table 12. In this table, the a number of ative subcarriers N_{active} is adopted for both FCC and ARIB regulations for covering the whole frequency band covered by these regulations described in [71]. Also, the whole CENELEC band is considered, i.e. from the lowest frequency of the CENELEC A band to the highest frequency of the CENELEC D band, being the adopted number of active subcarriers equal to the necessary for covering this whole frequency bandwidth.

Table 12: Adopted HS-OFDM-based TDR system parameters according to NB-PLC regulations.

HS-OFDM-based TDR system parameters				
		FCC	ARIB	CENELEC
Frequency range (kHz)		$10 - 490$	$10 - 450$	$3 - 1412.75$
Frequency bandwidth B (kHz)		480	440	145.5
Sampling frequency F_s (MHz)		1.2	1.2	0.4
FFT/IFFT size		256	256	256
Active subcarriers		$3 - 104$	$3 - 96$	$2 - 95$
Number of active subcarriers N_{active}		102	94	94
Cyclic prefix length L_{cp}	Standard	30	30	30
	Long	52	52	-

For HS-OFDM-based TDR systems parametrized according to these three regulations, Table 13 lists the achieved PSLR and ISLR values, as well as range resolution and maximum unambiguous range for the LV and MV scenarios from Table 2. Based on the data of this table, one can conclude that FCC and ARIB regulations allow a more appropriate sensing of shorter power distribution network sections than CENELEC, providing finer range resolution and shorter maximum unambiguous range. Also, adopting the long L_{cp} of both FCC and ARIB regulations results in a significant increase of $d_{\max}$ at the cost of obtaining less reflectograms over time due to the transmission of more cyclic prefix samples.

Table 13: Resulting range resolution and maximum unambiguous range in LV and MV scenarios, PSLR, and ISLR for NB-PLC regulations.

HS-OFDM-based TDR system aspects			FCC	ARIB	CENELEC
Range resolution Δd (m)	**LV**		78.07	85.17	257.56
	MV		133.59	145.73	440.70
Max. unamb. range $d_{\max}$ (km)	**Std. L_{cp}**	**LV**	1.87	1.87	5.62
		MV	3.21	3.21	9.62
	Long L_{cp}	**LV**	3.25	3.25	-
		MV	5.56	5.56	-
Sidelobe level	**PSLR (dB)**		-13.26	-13.26	-13.26
	ISLR (dB)		-9.66	-9.66	-9.66

APPENDIX C – List of Publications

The list of published journal papers during the graduate period is as follows:

- M. de L. Filomeno, G. R. Colen, L. G. de Oliveira, and M. V. Ribeiro, "Two-Stage Single-Relay Channel Model for In-Home Broadband PLC Systems," vol. 33, no. 1, pp. 204-214, Mar., 2019.

- L. G. de Oliveira, G. R. Colen, A. J. Han Vinck, and M. V. Ribeiro, "Resource Allocation in HS-OFDM-based PLC Systems: A Tutorial," *Journal of Communication and Information Systems*, vol. 33, no. 1, pp. 308-321, Oct., 2018.

The list of released preprints during the graduate period is as follows:

- L. G. de Oliveira, M. de L. Filomeno, L. F. Colla, H. V. Poor, and M. V. Ribeiro, "On the Suitability of PLC Pulses for Power Line Fault Sensing via Time-Domain Reflectometry," available at `https://arxiv.org/abs/1901.07923`, pp. 1-13, Jan. 2019.

- L. G. de Oliveira, M. de L. Filomeno, and M. V. Ribeiro, "HS-OFDM-based Time-Domain Reflectometry for Power Line Sensing: Characteristics and Limitations," available at `https://arxiv.org/abs/1901.08404`, pp. 1-12, Jan. 2019.

- L. G. de Oliveira, M. de L. Filomeno, and M. V. Ribeiro, "Orthogonal Chirp Division Multiplexing for Power Line Sensing via Time-Domain Reflectometry," available at `https://arxiv.org/abs/1901.09923`, pp. 1-8, Jan. 2019.